

# Monte Carlo Neural PDE Solver for Learning PDEs via Probabilistic Representation

Rui Zhang<sup>\*a</sup>, Qi Meng<sup>b</sup>, Rongchan Zhu<sup>c</sup>, Yue Wang<sup>b</sup>, Wenlei Shi<sup>b</sup>, Shihua Zhang<sup>a</sup>, Zhi-Ming Ma<sup>a</sup>, and Tie-Yan Liu<sup>b</sup>

<sup>a</sup>Academy of Mathematics and Systems Science, Chinese Academy of Sciences, Zhongguancun East Road, Beijing, China

<sup>b</sup>Microsoft Research, Danling Street, Haidian, Beijing, China

<sup>c</sup>Bielefeld University, Bielefeld, North Rhine-Westphalia, Germany

November 27, 2023

## Abstract

In scenarios with limited available or high-quality data, training the function-to-function neural PDE solver in an unsupervised manner is essential. However, the efficiency and accuracy of existing methods are constrained by the properties of numerical algorithms, such as finite difference and pseudo-spectral methods, integrated during the training stage. These methods necessitate careful spatiotemporal discretization to achieve reasonable accuracy, leading to significant computational challenges and inaccurate simulations, particularly in cases with substantial spatiotemporal variations. To address these limitations, we propose the Monte Carlo Neural PDE Solver (MCNP Solver) for training unsupervised neural solvers via the PDEs' probabilistic representation, which regards macroscopic phenomena as ensembles of random particles. Compared to other unsupervised methods, MCNP Solver naturally inherits the advantages of the Monte Carlo method, which is robust against spatiotemporal variations and can tolerate coarse step size. In simulating the random walk of particles, we employ Heun's method for the convection process and calculate the expectation via the probability density function of neighbouring grid points during the diffusion process. These techniques enhance accuracy and circumvent the computational memory and time issues associated with Monte Carlo sampling, offering an improvement over traditional Monte Carlo methods. Our numerical experiments on convection-diffusion, Allen-Cahn, and Navier-Stokes equations demonstrate significant improvements in accuracy and efficiency compared to other unsupervised baselines. The source code will be publicly available at: <https://github.com/optray/MCNP>.

## 1 Introduction

The function-to-function neural PDE solvers, which leverage neural networks as surrogate models to approximate the solutions of a family of PDEs, are emerging as a new paradigm for simulating physical systems with the development of deep learning [12, 25, 33, 35]. Along this direction,

---

<sup>\*</sup>This work was done when the author was visiting Microsoft Research. E-mail:{rayzhang@amss.ac.cn, meq@microsoft.com}

several studies have proposed diverse network architectures for neural PDE solvers [4, 32, 35]. These solvers can be trained using supervised [32, 35] or unsupervised approaches [34, 58, 64], employing pre-generated data or PDE information to construct training targets, respectively. The unsupervised training approach is essential for deep learning-based PDE solvers, particularly in scenarios with limited available or high-quality data. To address this issue, some studies [34, 58] borrow techniques from classical numerical solvers to construct training targets. For instance, the low-rank decomposition network (LordNet) [58] and physics-informed neural operator (PINO) [34] integrate finite difference or pseudo-spectral methods with neural networks during the training stage. However, these traditional Eulerian methods generally require fine meshes or step sizes for stable simulations. Therefore, the performance and efficiency of corresponding neural PDE solvers are also limited by time and space discretization, particularly when handling high spatiotemporal variations.

To this end, we introduce the **Monte Carlo Neural PDE Solver (MCNP Solver)**, a novel approach for training neural solvers from a probabilistic perspective, which views macroscopic phenomena as ensembles of random movements of microscopic particles [67]. For a PDE system with probabilistic representation, we construct the loss function of the MCNP Solver between two sequential PDE fields  $u_t$  and  $u_{t+\Delta t}$  via the relationship derived from the Monte Carlo approximation. To ensure the efficiency and accuracy of the MCNP Solver, we developed several techniques when combining the Monte Carlo approximation with the training of the deep neural network. Specifically, in simulating the corresponding stochastic difference equations (SDE), we use the Heun’s method to obtain a more accurate result when handling the convection process. During the diffusion process, we approximate the mathematical expectation via the probability density function (PDF) of neighbouring grid points to eliminate sampling amounts of particles in Monte Carlo methods.

Compared to other unsupervised neural solvers, such as LordNet [58] and PINO [34], the MCNP Solver naturally inherits the advantages of Monte Carlo methods. It can tolerate coarse step size [10, 40], thereby reducing training costs and accumulated errors arising from temporal discretization. Additionally, it can efficiently handle high-frequency spatial fields due to its derivative-free property [1, 36]. Moreover, the boundary conditions are automatically encoded into the stochastic process of particles [1, 36], eliminating the need to introduce extra loss terms to satisfy such constraints.

In summary, we make the following contributions:

1. We propose the MCNP Solver, an innovative unsupervised approach for training neural solvers that can be applied to PDE systems with probabilistic representation. We also devise several strategies to boost performance and efficiency during the convection and diffusion processes in SDE simulations.
2. Our experiments involving the convection-diffusion, Allen-Cahn, and Navier-Stokes equations demonstrate significant improvements in accuracy and efficiency over other unsupervised neural solvers, particularly for simulation tasks with complex spatiotemporal variations and coarse step sizes.
3. Beyond comparisons with unsupervised learning methods, we comprehensively compare the MCNP Solver with other widely-used PDE solvers, including the traditional Eulerian solver, Monte Carlo methods, and the supervised training approach. We delve into a detailed discussion on each method’s strengths, weaknesses, and application scopes.

The structure of this paper is as follows: Section 2 introduces related works on two types of neural PDE solvers. Section 3 provides a detailed overview of the probabilistic representation of the PDEs and the proposed MCNP Solver. Sections 4 and 5 present the experimental results of the MCNP Solver in comparison with unsupervised learning methods and other popular PDE

solvers, respectively. Finally, Section 6 summarizes our method, discusses its limitations and outlines potential future work.

## 2 Related Work

In this section, we introduce two primary categories of neural PDE solvers as follows. The first category is designed to learn a location-to-value mapping for a specific PDE, such as physics-informed neural networks (PINNs) [50]. The second category is designed to learn a function-to-function mapping for a family of PDEs, such as Fourier neural operator (FNO) and DeepONet [33, 35]. In this paper, we target the second task and aim to learn neural PDE solvers between functional spaces that can generalize to different PDE conditions over a distribution.

### 2.1 The Location-to-Value Neural PDE Solver

The location-to-value PDE solver utilizes the neural network to approximate the solution for a specific PDE with fixed initial and boundary conditions. The input of the neural network is the location and time  $(\mathbf{x}, t)$ , and the output is the corresponding solution  $u(\mathbf{x}, t)$ . To this end, PINNs have been proposed to construct the loss function using the equation and boundary residuals via the automatic differentiation regime. They are widely employed for solving forward or inverse problems [6, 11, 24, 50, 69]. Recently, PINNs have made significant progress in addressing scientific problems based on PDEs, including Navier-Stokes equations [22, 38, 51], Schrödinger equations [19, 29], Allen-Cahn equations [23, 39], and more. Instead of PINNs, some works utilize the probabilistic representation to train neural networks [14, 17, 68], which can efficiently handle high-dimensional or fractional PDEs [14, 16, 42, 52, 53]. Furthermore, some studies design loss functions based on other numerical methods, such as the finite volume method [2], finite element method [41, 43], and energy-based method [66]. Notably, the aforementioned location-to-value methods require retraining neural networks when encountering a PDE with new initial conditions, which can be time-consuming. In this paper, we aim to learn a function-to-function PDE solver that can generalize over a distribution.

### 2.2 The Function-to-Function Neural PDE Solver

This kind of neural PDE solver has been proposed to learn mappings between functional spaces, such as mapping a PDE’s initial condition to its solution [35]. Works like DeepONet [35] and its variants [15, 28, 56, 62] encode the initial conditions and queried locations using branch and trunk networks, respectively. Additionally, Fourier Neural Operator (FNO) [33] and its variants [31, 49, 61] explore learning the operator in Fourier space, an efficient approach for handling different frequency components. Several studies have employed graph neural networks [4, 32] or transformers [5, 30] as the backbone models of neural solvers to adapt to complex geometries. However, these methods require the supervision of ground truth data generated via accurate numerical solvers, which can be time-consuming in general. To this end, some studies aim to train the neural PDE solvers without the supervision of data [20, 34, 58, 64]. For example, [64] proposed PI-DeepONets, which utilize the PDE residuals to train DeepONets in an unsupervised way. Similarly, [20] proposed Meta-Auto-Decoder, a meta-learning approach to learn families of PDEs in the unsupervised regime. Furthermore, LordNet [58] and PINO [34] borrow techniques from traditional Eulerian methods, such as the finite difference and pseudo-spectral methods, and utilize the corresponding residuals as training loss, respectively. Compared to these unsupervised methods, the MCNP Solver incorporates physics information through the

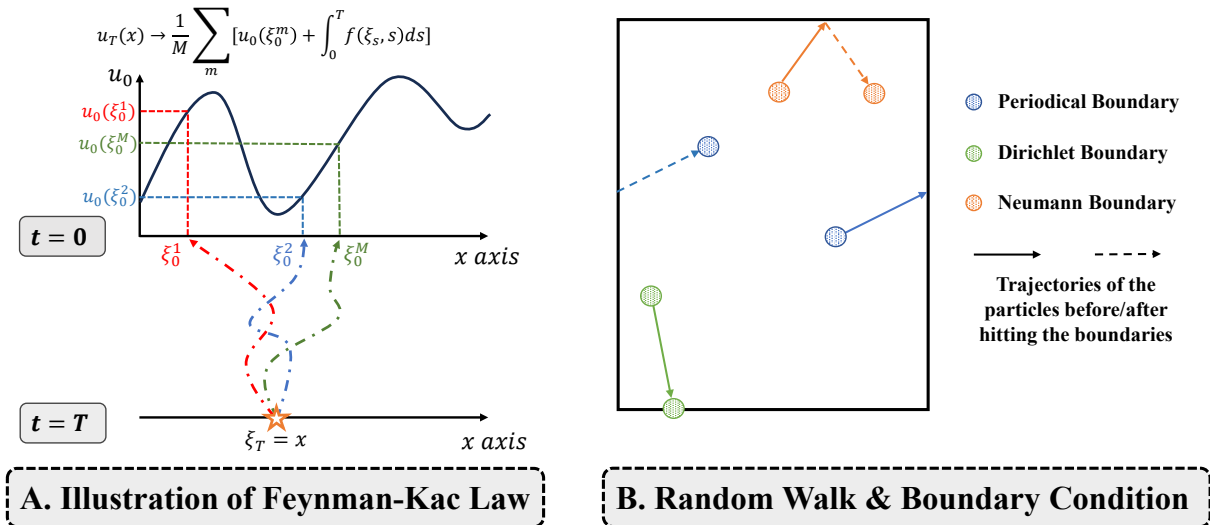


Figure 1: **Illustration of Feynman-Kac law and the random walks of particles when hitting different boundaries.** **A:**  $M$  particles  $\{\xi_s^m\}_{m=1}^M$  begin at the location  $\mathbf{x}$ , and conduct the random walk according to Eq. 4 from  $t = T$  to  $t = 0$ . When  $t = 0$ , the particles query the value at  $u_0$ , and their average value can be considered as the approximation of  $u_T(x)$  (Eq. 5). **B:** Monte Carlo methods can naturally encode boundary conditions in the random walk of particles. For periodical/Dirichlet/Neumann boundary conditions, the random walks of particles need to be pulled back/stopped/reflected when hitting the boundaries, respectively.

Feynman-Kac law, inheriting the advantage of Lagrangian methods. This approach allows the neural PDE solver to exhibit robustness against spatiotemporal variants, tolerate coarse step size, and naturally encode the boundary conditions.

### 3 Methodology

In this section, we introduce the methodology part of the proposed MCNP Solver. Section 3.1 introduces the Monte Carlo method and its corresponding theory, i.e., Feynman-Kac law. Section 3.2 presents the overall framework of the neural Monte Carlo loss, and Section 3.3 provides corresponding details in simulating the convection and diffusion processes in neural Monte Carlo loss.

#### 3.1 Preliminary

In this paper, we consider the general convection-diffusion equation defined as follows:

$$\begin{aligned} \frac{\partial u}{\partial t} &= \beta[u](\mathbf{x}, t) \cdot \nabla u + \kappa \Delta u + f(\mathbf{x}, t), \\ u(\mathbf{x}, 0) &= u_0(\mathbf{x}), \end{aligned} \tag{1}$$

where  $\mathbf{x} \in \Omega \subset \mathbb{R}^d$  and  $t$  denote the  $d$ -dimensional spatial variable and the time variable, respectively,  $\beta[u](\mathbf{x}, t) \in \mathbb{R}^d$  is a vector-valued mapping from  $(u, \mathbf{x}, t)$  to  $\mathbb{R}^d$ ,  $\kappa \in \mathbb{R}^+$  is the

diffusion parameter, and  $f(\mathbf{x}, t) \in \mathbb{R}$  denotes the force term. Many well-known PDEs, such as the Allen–Cahn and Navier-Stokes equations, can be viewed as a special form of Eq. 1.

For such PDEs with the form of Eq. 1, the Feynman-Kac formula provides the relationship between the PDEs and the corresponding probabilistic representation [16, 44, 45]. In detail, we can use the time inversion (i.e.,  $\tilde{u}(\mathbf{x}, t) = u(\mathbf{x}, T - t)$ ,  $\tilde{f}(\mathbf{x}, t) = f(\mathbf{x}, T - t)$ ) to the PDE as:

$$\begin{aligned} \frac{\partial \tilde{u}}{\partial t} &= -\beta[\tilde{u}](\mathbf{x}, t) \cdot \nabla \tilde{u} - \kappa \Delta \tilde{u} - \tilde{f}(\mathbf{x}, t), \\ \tilde{u}(\mathbf{x}, T) &= u_0(\mathbf{x}). \end{aligned} \quad (2)$$

Applying the Feynman-Kac formula [37] to the terminal value problem Eq. 2, we have

$$\tilde{u}_0(\mathbf{x}) = \mathbb{E} \left[ \tilde{u}_T(\tilde{\boldsymbol{\xi}}_T) + \int_0^T \tilde{f}(\tilde{\boldsymbol{\xi}}_s, s) ds \right], \quad (3)$$

where  $\tilde{\boldsymbol{\xi}}_s \in \mathbb{R}^d$  is a random process starting at  $\mathbf{x}$ , and moving from  $t = 0$  to  $t = T$ , which satisfies:

$$\begin{aligned} d\tilde{\boldsymbol{\xi}}_s &= \beta[\tilde{u}](\tilde{\boldsymbol{\xi}}_s, s) ds + \sqrt{2\kappa} d\mathbf{B}_s, \\ \tilde{\boldsymbol{\xi}}_0 &= \mathbf{x}, \end{aligned} \quad (4)$$

where  $\mathbf{B}_s$  is the  $d$ -dimensional standard Brownian motion. Applying time inversion  $t \rightarrow T - t$  to Eq. 3 and letting  $\boldsymbol{\xi}$  be the inversion of  $\tilde{\boldsymbol{\xi}}$ , we have

$$u_T(\mathbf{x}) = \mathbb{E}_{\boldsymbol{\xi}} \left[ u_0(\boldsymbol{\xi}_0) + \int_0^T f(\boldsymbol{\xi}_s, s) ds \right]. \quad (5)$$

We illustrate the diagram of Feynman-Kac law in the 1D case in Fig. 1.A, where the mathematical expectation in Eq. 5 can be naturally approximated via the Monte Carlo sampling. Feynman-Kac formula can automatically encode boundary conditions into the random walk of particles, including the periodical, Dirichlet and Neumann boundary conditions, as discussed in Fig. 1.B. Furthermore, apart from Eq. 1, some other PDEs can also be handled via the Feynman-Kac formula after specific processing, like wave equations [9] and spatially varying diffusion equations [55].

Based on the Feynman-Kac law, various Monte Carlo methods have been developed to solve PDEs with the form of Eq. 1 [7, 47]. For linear PDEs, Monte Carlo methods can directly simulate the corresponding SDEs and obtain the solution of the targeted PDEs with Eq. 5. For nonlinear PDEs (like Navier-Stokes and Allen-Cahn equations), we cannot simulate the SDEs in Eq. 4 or the mathematical expectation in Eq. 5 directly because the unknown  $u$  is required during the simulation. To this end, some advanced numerical algorithms have been developed, such as the random vortex method [48] and the branching diffusion method [18]. Compared to the traditional Eulerian methods, Monte Carlo methods are more adaptable to significant spatiotemporal variations due to their Lagrangian nature, which is widely used for simulating the breaking wave and turbulent problems [21, 26]. Moreover, Monte Carlo methods have been proven to be less restrictive in terms of step size constraints via the analysis of the Courant number [8, 54]. However, the accuracy of Monte Carlo methods is limited by the number of particles, which can introduce severe computational time and memory issues [40]. In the following, we will introduce the MCNP Solver, which could be efficiently trained while inheriting the advantages of the Monte Carlo simulation method.

### 3.2 Neural Monte Carlo Loss

Given a PDE in the form of Eq. 1 and the distribution of the initial conditions  $\mathcal{D}_0$ , the objective of MCNP Solver is to learn a functional mapping  $\mathcal{G}_\theta$  with parameter  $\theta$  that can simulate the

subsequent fields for all the initial fields  $u_0 \sim \mathcal{D}_0$  at time  $t \in [0, T]$ . The inputs and outputs of  $\mathcal{G}_\theta$  are given as:

$$\begin{aligned} \mathcal{G}_\theta : \mathcal{D}_0 \times [0, T] &\rightarrow \mathcal{D}_{[0, T]}, \\ (u_0, t) &\mapsto u_t, \end{aligned} \quad (6)$$

where  $\mathcal{D}_{[0, T]}$  denotes the joint distribution of the field after  $t = 0$ . In this paper, we are interested in the evolution of PDEs at fixed coordinate system  $\{\mathbf{x}_p\}_{p=1}^P \in \Omega$ , which aligns with the settings in [4, 33]. Consequently, the inputs and outputs of the solver  $\mathcal{G}_\theta$  are solution values at  $P$  grid points, i.e., each  $u_t$  is represented by a  $P$ -dimensional vector  $[u_t(\mathbf{x}_1), \dots, u_t(\mathbf{x}_P)]$ .

In practice, we use the deep neural network models [33] to construct the mapping  $\mathcal{G}_\theta$  and the trained network served as the MCNP Solver. Unlike other supervised learning algorithms [4, 33, 35], MCNP Solver is trained in an unsupervised way, i.e., only utilizing the physics information provided by PDEs. To this end, we consider training the solver via the relationship between  $u_t$  and  $u_{t+\Delta t}$  (where  $0 \leq t < t+\Delta t \leq T$ ) derived by the aforementioned probabilistic representation. Considering Eq. 5, an expected neural PDE solver  $\mathcal{G}_\theta$  should satisfy the following equation at each  $\mathbf{x}_p$ :

$$\begin{aligned} &\mathcal{G}_\theta(u_0, t + \Delta t)(\mathbf{x}_p) \\ &= \mathbb{E}_{\xi_p} \left[ \mathcal{G}_\theta(u_0, t)(\xi_{p,t}) + \int_t^{t+\Delta t} f(\xi_{p,s}, s) ds \right], \end{aligned} \quad (7)$$

where  $\xi_{p,s}$  ( $s \in [t, t + \Delta t]$ ) is the inverse version of stochastic process in Eq. 4 as follows:

$$\begin{aligned} d\xi_{p,s} &= -\beta[u](\xi_{p,s}, s) ds - \sqrt{2\kappa} d\mathbf{B}_s, \\ \xi_{p,t+\Delta t} &= \mathbf{x}_p. \end{aligned} \quad (8)$$

Regarding Eq. 7 as the optimization objective, the neural Monte Carlo loss can be written as follows:

$$\begin{aligned} \mathcal{L}_{\text{MCNP}}(\mathcal{G}_\theta|u_0) &= \sum_{t=0}^{T-\Delta t} \sum_{p=1}^P \left\| \mathcal{G}_\theta(u_0, t + \Delta t)(\mathbf{x}_p) - \right. \\ &\quad \left. \mathbb{E}_{\xi_p} \left[ \mathcal{G}_\theta(u_0, t)(\xi_{p,t}) + \int_t^{t+\Delta t} f(\xi_{p,s}, s) ds \right] \right\|_2, \end{aligned} \quad (9)$$

where  $\mathcal{G}_\theta(u_0, 0)$  is directly set to be  $u_0$  in experiments. During the training stage, we uniformly sample  $B$  initial states  $u_0$  from  $\mathcal{D}_0$  per epoch to ensure the generalizability of the learned MCNP Solver.

### 3.3 The Simulation of SDE

When calculating the loss function defined in Eq. 9, a crucial step is to approximate the expectation over random samples  $\xi_p$  via simulating the SDE in Eq. 8. Classical Euler–Maruyama method [63] has been adopted to approximate corresponding SDEs [16, 42], i.e.,

$$\begin{aligned} \xi_{p,t}^m &= \xi_{p,t+\Delta t} + \underbrace{\beta[u](\xi_{p,t+\Delta t}, t + \Delta t)\Delta t}_{\text{convection}} + \underbrace{\sqrt{2\kappa\Delta t}\mathbf{b}^m}_{\text{diffusion}}, \\ \mathbf{b}^m &\sim \mathcal{N}(\mathbf{0}, \mathbf{I}), \quad \xi_{p,t+\Delta t} = \mathbf{x}_p, \end{aligned} \quad (10)$$

where the physical meaning of  $\beta[u](\xi_{p,t+\Delta t}, t + \Delta t)\Delta t$  and  $\sqrt{2\kappa\Delta t}\mathbf{b}^m$  denote the convection and diffusion processes, respectively. After sampling  $M$  particles  $\{\xi_{p,t}^m\}_{m=1}^M$ , the training target in Eq. 7 can be approximated via the Monte Carlo method, i.e.,

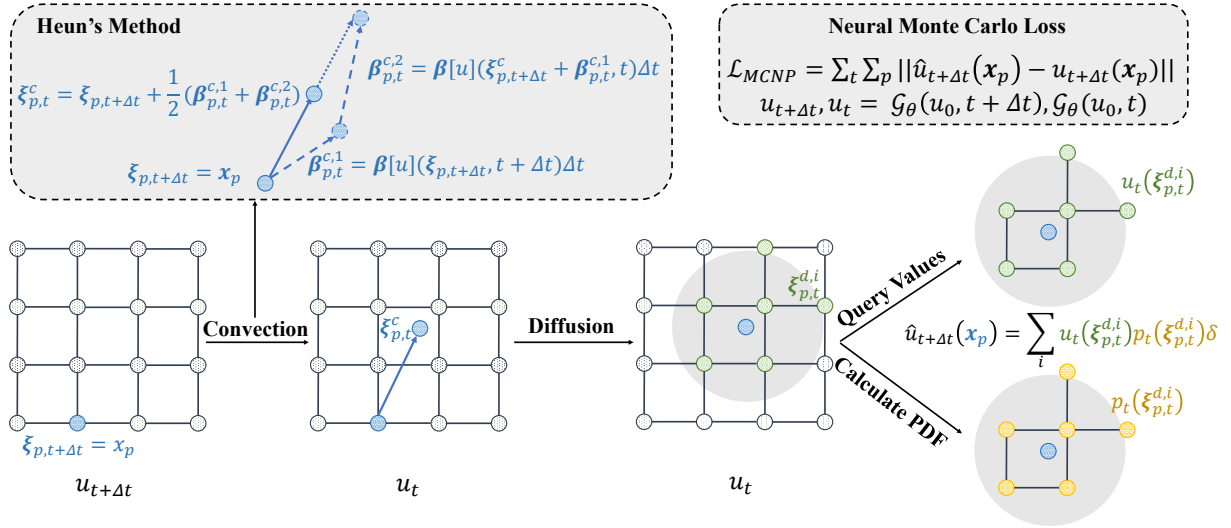


Figure 2: **Illustration of the neural Monte Carlo loss.** We construct the training loss via the relationship between  $u_t$  and  $u_{t+\Delta t}$  given by the Feynman-Kac law. Given a grid point at  $x_p$ , we split the random walk in Eq. 10 as the convection and diffusion parts. For the convection process, we utilize the Heun’s method to simulate the particle moving from time  $t + \Delta t$  to  $t$  driven by the drift term  $\beta$ . For the diffusion process, we calculate the mathematical expectation in Eq. 7 through the probability density function (PDF) of neighbouring grid points when handling the diffusion process to eliminate sampling using Monte Carlo methods, where  $p_t(\xi_{p,t}^{d,i})$  denotes the transition probability for the particle moving from  $\xi_{p,t}^c$  to  $\xi_{p,t}^{d,i}$  driven by the diffusion effect. Please note that we omit external forcing  $f$  in the figure for simplification.

$$\hat{u}_{t+\Delta t}(x_p) \approx \frac{1}{M} \sum_{m=1}^M [u_t(\xi_{p,t}^m) + f(\xi_{p,t+\Delta t}, t + \Delta t)\Delta t]. \quad (11)$$

The selection of the simulation algorithm significantly impacts the efficiency of the training process and the accuracy of the trained solver. This necessitates a careful design approach that considers both the approximation error and the training efficiency, such as computational time and memory. On the one hand, to reduce the discretization error when dealing with the convection term, we consider a higher-order approximation scheme. On the other hand, sampling amounts of particles to calculate the diffusion term will introduce severe computational issues, especially when the diffusive rate  $\kappa$  is high. As a result, we explore a method that avoids sampling of the particles during the diffusion process.

In the subsequent sections, we will introduce two methods, including: 1). Utilize Heun’s method to obtain a more accurate approximation of the convection process; 2). Calculate the mathematical expectation via the probability density function (PDF) of neighbouring grid points when handling the diffusion process to eliminate the sampling in Monte Carlo methods, as shown in Fig. 2.

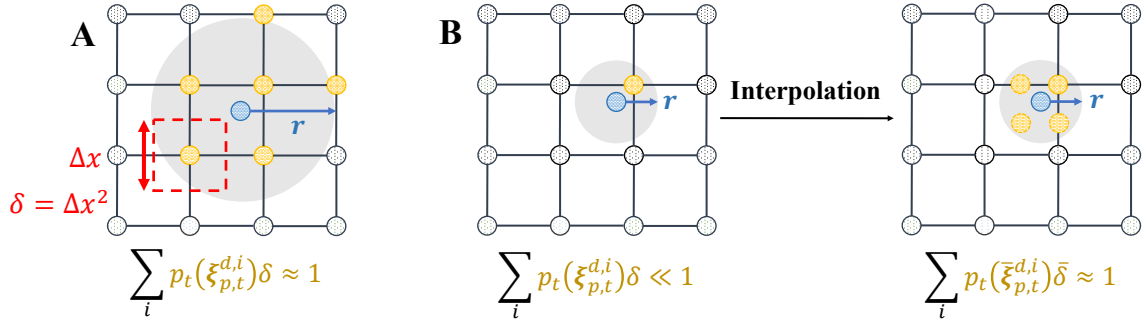


Figure 3: **The Choice of Neighbourhood Radius  $r$**  **A:** We first choose the smallest possible value of  $r$  that satisfies Eq. 17. If we have  $\sum_i p_t(\xi_{p,t}^{d,i})\delta \approx 1$ , using Eq. 15 directly to approximate the corresponding mathematical expectation can reduce computational cost while ensuring accuracy.  $\delta$  denotes the volume of each cell (as shown in the red box) in the coordinate system. **B:** When the grid size is close to the radius  $r$ , we may encounter the scenario that  $\sum_i p_t(\xi_{p,t}^{d,i})\delta \ll 1$ . To address this issue, we interpolate the coordinate system to a high-resolution one to satisfy the normalization condition in Eq. 17.  $\bar{\delta}$  denotes the volume of each cell in the high-resolution coordinate system.

### 3.3.1 The Simulation of Convection Process

We aim to approximate the location of  $\xi_{p,s}$  moving back to time  $t$  with the convection effect, i.e.,  $\xi_{p,t}^c \triangleq \xi_{p,t+\Delta t} + \int_t^{t+\Delta t} \beta[u](\xi_{p,s}, s)ds$ . To obtain a more accurate result, we replace the classical Euler scheme with Heun's method, which calculates the intermediate location before the final approximation. The complete mathematical expression can be written as follows:

$$\begin{aligned}
 \beta_{p,t}^{c,1} &= \beta[u](\xi_{p,t+\Delta t}, t + \Delta t) \Delta t; \\
 \beta_{p,t}^{c,2} &= \beta[u](\xi_{p,t}^c + \beta_{p,t}^{c,1}, t) \Delta t; \\
 \xi_{p,t}^c &= \xi_{p,t+\Delta t} + \frac{1}{2} (\beta_{p,t}^{c,1} + \beta_{p,t}^{c,2}),
 \end{aligned} \tag{12}$$

where  $u$  is the output of the MCNP Solver in each iteration.

### 3.3.2 The Simulation of Diffusion Process

Unlike the Euler-Maruyama method, which samples  $M$  particles to simulate the diffusion process, we calculate the mathematical expectation via the PDF of neighbouring grid points to replace the sampling in Monte Carlo methods. Given  $\xi_{p,t}^c$ , which represents the location of particles after the convection process (Eq. 12), we first find its neighbourhood  $N(\xi_{p,t}^c, r)$  from the coordinates as follows:

$$N(\xi_{p,t}^c, r) \triangleq \{\xi_{p,t}^{d,i} : \|\xi_{p,t}^{d,i} - \xi_{p,t}^c\|_2 \leq r, \xi_{p,t}^{d,i} \in \{\mathbf{x}_p\}_{p=1}^P\}, \tag{13}$$

where  $r > 0$  represents the radius of the neighbourhood. Considering the transition probability for  $\xi_{p,t}^c$  moving to its neighbour  $\xi_{p,t}^{d,i} \in N(\xi_{p,t}^c, r)$ , we can calculate the analytical form of the corresponding PDF as follows:

$$p_t(\xi_{p,t}^{d,i}) = \frac{1}{(2\pi\sigma^2)^{d/2}} \exp\left(-\frac{\|\xi_{p,t}^{d,i} - \xi_{p,t}^c\|_2^2}{2\sigma^2}\right), \tag{14}$$

where  $\sigma = \sqrt{2\kappa\Delta t}$  denotes the standard deviation of the Brownian motion in Eq. 8. Please note that in Eq. 14, we assume that the particles will not hit the boundary by default. When the particle  $\boldsymbol{\xi}_{p,t}^c$  has the possibility of hitting the boundary, we need to modify the PDF in Eq. 14 to the corresponding form. For instance, the PDF corresponds to the Brownian motion with absorption/reflection when we handle the Dirichlet/Neumann boundary conditions, respectively. We use the grid points inside the neighbourhood to approximate the mathematical expectation in Eq. 7 as follows:

$$\begin{aligned} & \mathbb{E}_{\boldsymbol{\xi}_p} [\mathcal{G}_\theta(u_0, t)(\boldsymbol{\xi}_{p,t})] \\ & \approx \sum_{\boldsymbol{\xi}_{p,t}^{d,i} \in N(\boldsymbol{\xi}_{p,t}^c, r)} \mathcal{G}_\theta(u_0, t)(\boldsymbol{\xi}_{p,t}^{d,i}) \cdot p_t(\boldsymbol{\xi}_{p,t}^{d,i}) \cdot \delta, \end{aligned} \quad (15)$$

where we use the density value at point  $\boldsymbol{\xi}_{p,t}^{d,i}$  to approximate the density of the cells centered on  $\boldsymbol{\xi}_{p,t}^{d,i}$  (the red box in Fig. 3.A) and  $\delta$  denotes the volume of each cell. We utilize a similar way to calculate the integration of the external forcing  $f$  in Eq. 7 as follows:

$$\begin{aligned} & \mathbb{E}_{\boldsymbol{\xi}_p} \left[ \int_t^{t+\Delta t} f(\boldsymbol{\xi}_{p,s}, s) ds \right] \\ & \approx \frac{\Delta t}{2} \left[ f(\boldsymbol{\xi}_{p,t+\Delta t}, t + \Delta t) + \sum_{\boldsymbol{\xi}_{p,t}^{d,i} \in N(\boldsymbol{\xi}_{p,t}^c, r)} f(\boldsymbol{\xi}_{p,t}^{d,i}, t) p_t(\boldsymbol{\xi}_{p,t}^{d,i}) \right]. \end{aligned} \quad (16)$$

### 3.3.3 The Choice of Neighbourhood Radius $r$

In Eq. 15, we utilize the grid points located in the neighbourhood  $N(\boldsymbol{\xi}_{p,t}^c, r)$  to approximate the corresponding mathematical expectation. To ensure the approximation error is under control, we hope the accumulated probability of the points in the range will approach 1, i.e., given a sufficiently small  $\epsilon$ , we hope the radius  $r$  satisfies the following conditions:

$$\begin{aligned} & r = \arg \min \gamma, \\ & \text{s.t.}, \int_{\|\boldsymbol{\xi} - \boldsymbol{\xi}_{p,t}^c\|_2 \leq \gamma} p_t(\boldsymbol{\xi}) d\boldsymbol{\xi} \geq 1 - \epsilon. \end{aligned} \quad (17)$$

The radius  $r$  in Eq. 17 represents the minimum scope where particles can be covered with a probability close to 1 during the diffusion process. After choosing the radius  $r$ , we use the neighbouring grid points to calculate the corresponding mathematical expectation via Eq. 15, which can be accurately approximated with minimal computational cost when  $\sum_i p_t(\boldsymbol{\xi}_{p,t}^{d,i}) \delta \approx 1$ . However, when the grid size is close to the radius  $r$ , we may encounter  $\sum_i p_t(\boldsymbol{\xi}_{p,t}^{d,i}) \delta \ll 1$  because the random walks of particles are concentrated around  $\boldsymbol{\xi}_{p,t}^c$  while the grid points are not dense enough. To address this issue, we interpolate the coordinate system  $\{\boldsymbol{x}_p\}_{p=1}^P$  to a high-resolution one  $\{\bar{\boldsymbol{x}}_p\}_{p=1}^P$  (yellow points in Fig. 3.B), such that  $\sum_i p_t(\bar{\boldsymbol{\xi}}_{p,t}^{d,i}) \bar{\delta} \approx 1$ , where  $\bar{\delta}$  is the volume of each cell in the high-resolution coordinate system and  $\bar{\boldsymbol{\xi}}_{p,t}^{d,i}$  located in the neighbourhood  $\bar{N}(\boldsymbol{\xi}_{p,t}^c, r)$  defined as:

$$\bar{N}(\boldsymbol{\xi}_{p,t}^c, r) \triangleq \{\bar{\boldsymbol{\xi}}_{p,t}^{d,i} : \|\bar{\boldsymbol{\xi}}_{p,t}^{d,i} - \boldsymbol{\xi}_{p,t}^c\|_2 \leq r, \bar{\boldsymbol{\xi}}_{p,t}^{d,i} \in \{\bar{\boldsymbol{x}}_p\}_{p=1}^P\}. \quad (18)$$

After that, we approximate the expectation in Eq. 7 in the high-resolution coordinate system as in Eq. 15. Please note that we only have access to the value of  $\mathcal{G}_\theta(u_0, t)$  in the low-resolution coordinate system directly, and thus we need to interpolate the physical field  $\mathcal{G}_\theta(u_0, t)$  to the corresponding resolution. In practice, we utilize the Fourier transform to map the low-resolution PDE fields to the frequency domain, and use the inverse Fourier transform to remap it to the

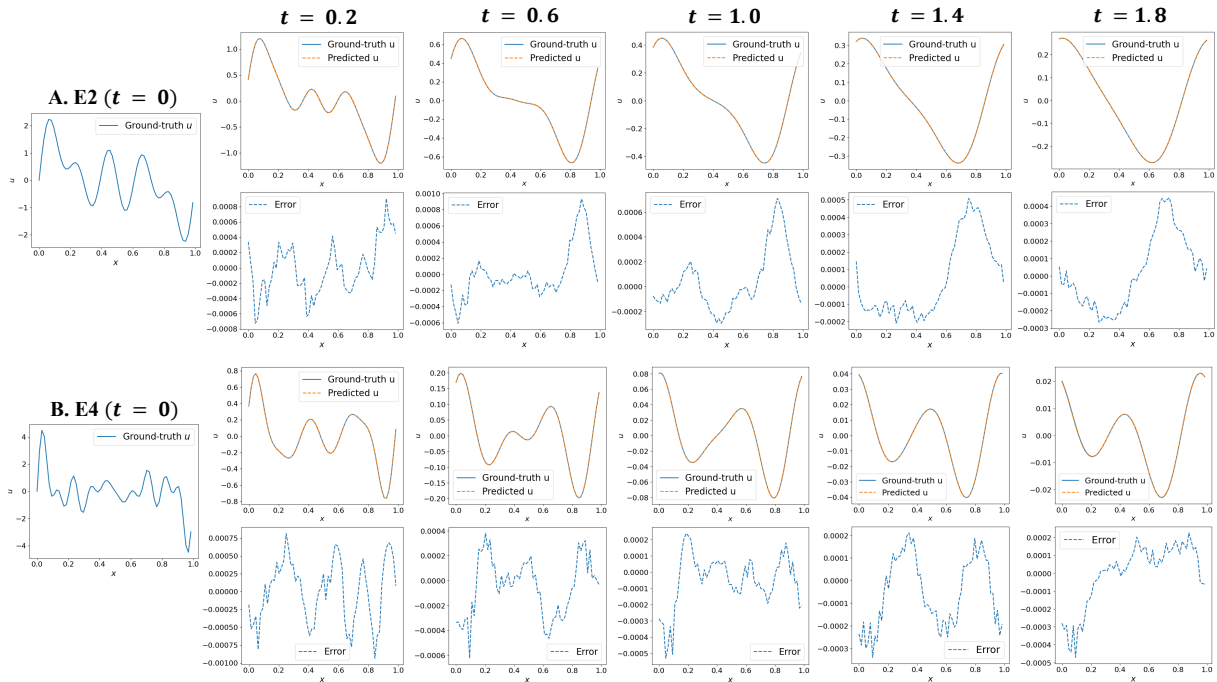


Figure 4: **Simulation of 1D convection-diffusion equation.** The ground truth solution versus the prediction of a learned MCNP-10 for an example in the test set at  $t = \{0.2, 0.6, 1.0, 1.4, 1.8\}$ , with  $(\kappa, N) = (0.01, 5)$  (A) and  $(0.01, 10)$  (B), respectively.

high-resolution space. We illustrate the choice of  $r$  and the interpolation trick of the MCNP Solver in Fig. 3.

## 4 Experiments

In this section, we conduct numerical experiments to evaluate the proposed MCNP Solver on three tasks: 1D convection-diffusion equation, 1D Allen-Cahn equation, and 2D Navier-Stokes equation. We introduce the implementation details of each baseline method and the generalization scheme of the test data in Appendix I. We utilize the FNO [33] as the backbone network for MCNP Solver and PINO [34]. For each task, we divide the time interval into 10 uniform frames, and evaluate the model performance via the average relative  $\ell_2$  error ( $E_{\ell_2}$ ) and relative  $\ell_\infty$  error ( $E_{\ell_\infty}$ ) over 10 frames on 200 test PDE samples. We repeat each experiment with three random seeds in  $\{0, 1, 2\}$  and report the mean value and variance. All experiments are implemented on an NVIDIA RTX 3090 GPU.

### 4.1 1D Convection-Diffusion Equation

In this section, we conduct experiments on periodical 1D convection-diffusion equation defined as follows:

$$\frac{\partial u(x, t)}{\partial t} = \beta \nabla u(x, t) + \kappa \Delta u(x, t), \quad x \in [0, 1], t \in [0, 2]. \quad (19)$$

Table 1: **1D convection-diffusion equation with varying  $N$  and  $\kappa$ .** Relative  $\ell_2$  errors ( $E_{\ell_2}$ ), relative  $\ell_\infty$  errors ( $E_{\ell_\infty}$ ) and computational costs for baseline methods and MCNP Solver. The best results are marked in bold, and the second best results are underlined.

Task	Model	$E_{\ell_2}$ (%)	$E_{\ell_\infty}$ (%)	Train Time (H)	Params (M)
E1 ( $\kappa = 0.005, N = 5$ )	PINO-10	3.919 $\pm$ 0.025	4.526 $\pm$ 0.155	0.034	0.140
	PINO-20	1.106 $\pm$ 0.010	1.318 $\pm$ 0.023	0.054	0.140
	PINO-100	0.222 $\pm$ 0.015	0.268 $\pm$ 0.017	0.257	0.140
	PI-DeepONet	0.706 $\pm$ 0.113	0.968 $\pm$ 0.114	0.086	0.153
	MCNP-10	<b>0.172 <math>\pm</math>0.018</b>	<b>0.222 <math>\pm</math>0.018</b>	0.032	0.140
	MCNP-20	<u>0.185 <math>\pm</math>0.010</u>	<u>0.235 <math>\pm</math>0.013</u>	0.054	0.140
E2 ( $\kappa = 0.01, N = 5$ )	PINO-10	4.784 $\pm$ 0.031	5.868 $\pm$ 0.072	0.034	0.140
	PINO-20	1.435 $\pm$ 0.005	1.720 $\pm$ 0.008	0.054	0.140
	PINO-100	0.328 $\pm$ 0.065	0.385 $\pm$ 0.063	0.257	0.140
	PI-DeepONet	1.440 $\pm$ 0.410	1.921 $\pm$ 0.424	0.097	0.153
	MCNP-10	<b>0.200 <math>\pm</math>0.012</b>	<b>0.259 <math>\pm</math>0.012</b>	0.032	0.140
	MCNP-20	<u>0.248 <math>\pm</math>0.025</u>	<u>0.307 <math>\pm</math>0.024</u>	0.054	0.140
E3 ( $\kappa = 0.005, N = 10$ )	PINO-10	5.444 $\pm$ 0.017	7.672 $\pm$ 0.123	0.035	0.173
	PINO-20	1.695 $\pm$ 0.008	2.392 $\pm$ 0.039	0.057	0.173
	PINO-100	0.349 $\pm$ 0.086	0.438 $\pm$ 0.097	0.269	0.173
	PI-DeepONet	3.729 $\pm$ 1.235	5.058 $\pm$ 1.661	0.097	0.199
	MCNP-10	<b>0.160 <math>\pm</math>0.006</b>	<b>0.239 <math>\pm</math>0.005</b>	0.033	0.173
	MCNP-20	<u>0.195 <math>\pm</math>0.020</u>	<u>0.244 <math>\pm</math>0.023</u>	0.056	0.173
E4 ( $\kappa = 0.01, N = 10$ )	PINO-10	5.754 $\pm$ 0.074	8.615 $\pm$ 0.152	0.035	0.173
	PINO-20	1.758 $\pm$ 0.022	2.589 $\pm$ 0.021	0.057	0.173
	PINO-100	0.964 $\pm$ 0.461	1.130 $\pm$ 0.537	0.269	0.173
	PI-DeepONet	5.219 $\pm$ 0.686	7.431 $\pm$ 1.354	0.086	0.199
	MCNP-10	<b>0.182 <math>\pm</math>0.021</b>	<b>0.233 <math>\pm</math>0.021</b>	0.033	0.173
	MCNP-20	<u>0.197 <math>\pm</math>0.008</u>	<u>0.246 <math>\pm</math>0.009</u>	0.056	0.173

The initial states  $u(x, 0)$  are generated from the functional space  $\mathcal{F}_N \triangleq \{\sum_{n=1}^N a_n \sin(2\pi n x) : a_n \sim \mathbb{U}(0, 1)\}$ , where  $\mathbb{U}(0, 1)$  denotes the uniform distribution over  $(0, 1)$ , and  $N$  represents the maximum frequency of the functional space.

#### 4.1.1 Experimental Settings

In this setting,  $\kappa$  represents the heat transfer rate, with larger  $\kappa$  values indicating faster temporal variation rates.  $N$  can be regarded as a measure of spatial complexity, where higher values correspond to a higher proportion of high-frequency signals. We select two different  $\kappa$  in  $\{0.005, 0.01\}$  and  $N$  in  $\{5, 10\}$ , respectively, to evaluate the performance of different methods in handling spatiotemporal variations. These four experimental settings are denoted E1/E2/E3/E4 with  $(\kappa, N) = (0.005, 5), (0.01, 5), (0.005, 10), (0.01, 10)$ , respectively. In this section, we set the convection coefficient  $\beta$  as 0.1. We divide the spatial domain  $[0, 1)$  into 64 grid elements for all experiments.

### 4.1.2 Baselines

We introduce the neural PDE solvers performed on 1D convection-diffusion equations, including: i). **PINO** [34]: An unsupervised neural operator. To evaluate the performance of PINO with varying step sizes, we divide the time interval into 10/20/100 uniform frames, denoted as PINO-10/20/100, respectively. The loss function is constructed through the pseudo-spectral method due to the periodical boundary condition; thus, the boundary conditions can be naturally satisfied. ii). **PI-DeepONet** [64]: an unsupervised neural operator based on PINN loss and DeepONets, which utilize the residual of PDE to construct the loss function. iii). **MCNP Solver**, we divide the time interval into 10/20 uniform frames, which are denoted as MCNP-10/20, respectively.

### 4.1.3 Results

Fig. 4 shows the ground truth versus the predicted  $u$  of MCNP-10 from  $t = 0.2$  to  $t = 1.0$  with  $(\kappa, N) = (0.01, 5)$  and  $(0.01, 10)$ , respectively. We can observe that higher  $N$  values can introduce more obvious spatial variations. Table 1 presents each method’s performance and computational cost in the 1D convection-diffusion equation. Among all unsupervised neural PDE solvers, including PI-DeepONet and PINO-10/20/100, the MCNP-10 performs the best on all tasks, particularly for cases with large spatial and temporal variations. The results of PI-DeepONet indicate that the PINN loss cannot efficiently handle high-frequency components, which has also been observed in previous literature [27, 65]. For PINO, its accuracy is not robust with step size, especially for cases with  $N = 10$ , indicating that the pseudo-spectral method cannot provide sufficiently accurate training targets with a coarser partition of the time interval. For PINO-100, despite achieving comparable results on E1, its training cost is more than eight times that of MCNP-10. Moreover, its relative  $\ell_2$  error increases by 334 % from E1 to E4, while MCNP-10 only increases by 6 %. It is also interesting to note that MCNP-10 performs better than MCNP-20 in Table 1, because the setting  $\Delta t = 2/10$  is already sufficient to provide accurate training signals for MCNP Solver in the convection-diffusion equation, while further refining the step size would only add additional fitting and generalization burdens.

## 4.2 1D Allen-Cahn Equation

In this section, we conduct experiments on the 1D Allen-Cahn equation with Dirichlet/Neumann boundary conditions as follows:

$$\begin{aligned} \frac{\partial u(x, t)}{\partial t} &= 0.01 \Delta u(x, t) + u(x, t) - u(x, t)^3, \\ x &\in [0, 1], t \in [0, 1]; \\ \text{Dirichlet: } &u(0, t) = u(1, t) = 0; \\ \text{Neuman: } &\frac{\partial u(x, t)}{\partial x} \Big|_{x=0} = \frac{\partial u(x, t)}{\partial x} \Big|_{x=1} = 0; \end{aligned} \tag{20}$$

The initial states  $u(x, 0)$  are generated from the functional space  $\mathcal{F}_N \triangleq \{\sum_{n=1}^N a_n \sin(2\pi n x) : a_n \sim \mathbb{U}(0, 1)\}$ , and  $N$  represents the maximum frequency of the functional space.

### 4.2.1 Experimental Settings

In this section, we select two different  $N$  in  $\{5, 10\}$  and two kinds of boundary conditions, respectively, to evaluate the performance of different methods in handling spatial variations and

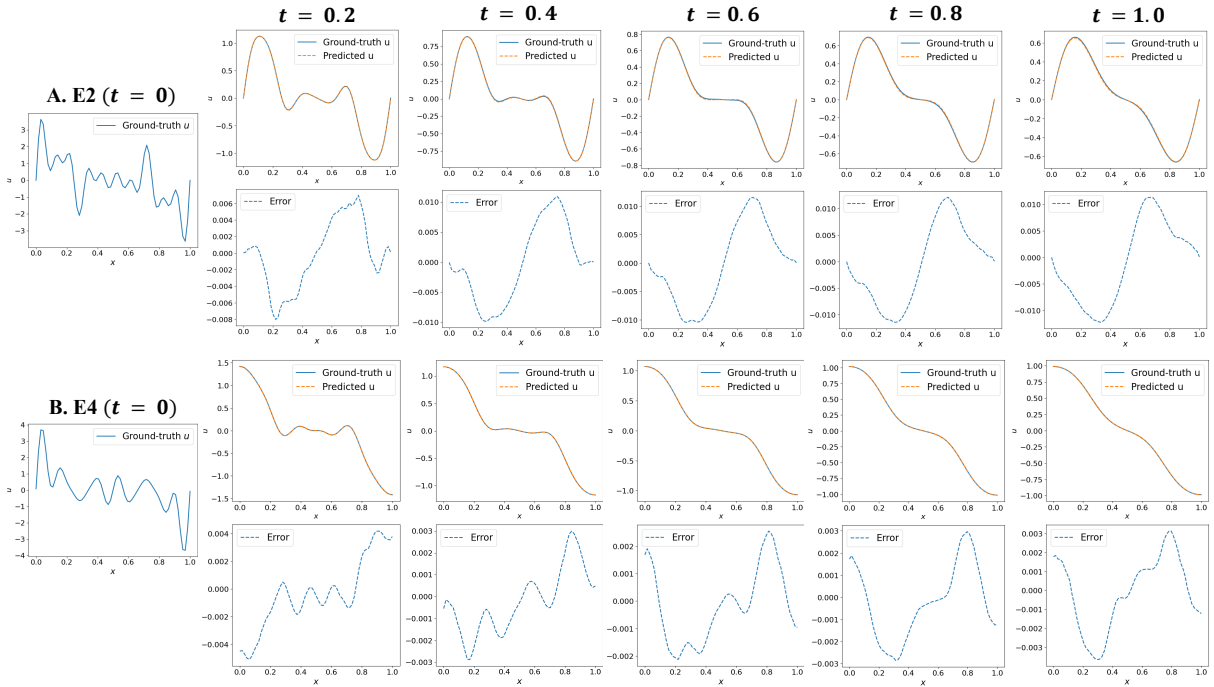


Figure 5: **Simulation of 1D Allen-Cahn equation.** The ground truth solution versus the prediction of a learned MCNP-100 for an example in the test set from  $t = 0.2$  to  $t = 1.0$ , with Dirichlet (E2, **A**) and Neumann (E4, **B**) boundary condition, respectively.

varying boundary conditions. These four experimental settings are denoted E1/E2/E3/E4 with  $(N, \text{Boundary}) = (5, \text{Dirichlet}), (10, \text{Dirichlet}), (5, \text{Neumann}), (10, \text{Neumann})$ , respectively. We divide the spatial domain  $[0, 1]$  into 65 uniform grid elements for all experiments.

#### 4.2.2 Baselines

We introduce the neural PDE solvers performed on the 1D Allen-Cahn equations, including: i). **PINO** [34]: An unsupervised neural operator. We divide the time interval into 20/100 uniform frames, denoted as PINO-20/100, respectively. The loss function is constructed through the finite difference method, and an additional loss term is involved in enforcing the neural PDE solver that satisfies the boundary conditions. ii). **PI-DeepONet** [64]: an unsupervised neural operator based on PINN loss and DeepONets. iii). **MCNP Solver**, we divide the time interval into 20/100 uniform frames, denoted as MCNP-20/100, respectively.

#### 4.2.3 Results

Fig. 5 shows the comparison between the ground truth and predicted  $u$  of MCNP Solver from  $t = 0.2$  to  $t = 1.0$  with Dirichlet and Neumann boundary conditions, respectively. The simulation of the Allen-Cahn equation is more challenging than the convection-diffusion equation due to its nonlinear nature. Table 2 presents each method’s performance and computational cost in the 1D Allen-Cahn equation. Among all unsupervised methods, only MCNP-100 achieves a relative error lower than 1 % on all experiments and metrics. Unlike PINO, which requires an extra loss

Table 2: **1D Allen-Cahn equation with varying  $N$  and boundary conditions.** Relative  $\ell_2$  errors ( $E_{\ell_2}$ ), relative  $\ell_\infty$  errors ( $E_{\ell_\infty}$ ) and computational costs for baseline methods and MCNP Solver. The best results are marked in bold, and the second best results are underlined.

Task	Model	$E_{\ell_2}$ (%)	$E_{\ell_\infty}$ (%)	Train Time (H)	Params (M)
E1 ( $N = 5$ , Dirichlet)	PINO-20	1.707 $\pm$ 0.262	2.082 $\pm$ 0.271	0.135	0.140
	PINO-100	<u>0.639 <math>\pm</math>0.020</u>	<u>0.736 <math>\pm</math>0.009</u>	0.627	0.140
	PI-DeepONet	2.444 $\pm$ 1.022	3.551 $\pm$ 1.579	0.431	0.173
	MCNP-20	0.918 $\pm$ 0.037	1.108 $\pm$ 0.034	0.133	0.140
	MCNP-100	<b>0.547 <math>\pm</math>0.053</b>	<b>0.636 <math>\pm</math>0.061</b>	0.621	0.140
E2 ( $N = 10$ , Dirichlet)	PINO-20	3.180 $\pm$ 0.182	4.534 $\pm$ 0.232	0.135	0.140
	PINO-100	<u>1.165 <math>\pm</math>0.192</u>	<u>1.430 <math>\pm</math>0.192</u>	0.627	0.140
	PI-DeepONet	5.615 $\pm$ 1.191	7.163 $\pm$ 1.455	0.431	0.173
	MCNP-20	1.290 $\pm$ 0.062	1.592 $\pm$ 0.079	0.133	0.140
	MCNP-100	<b>0.831 <math>\pm</math>0.200</b>	<b>0.955 <math>\pm</math>0.212</b>	0.621	0.140
E3 ( $N = 5$ , Neumann)	PINO-20	1.727 $\pm$ 0.368	2.885 $\pm$ 0.043	0.136	0.140
	PINO-100	1.705 $\pm$ 0.019	2.768 $\pm$ 0.043	0.627	0.140
	PI-DeepONet	1.773 $\pm$ 0.890	2.353 $\pm$ 1.128	0.433	0.173
	MCNP-20	<u>0.598 <math>\pm</math>0.011</u>	<u>0.801 <math>\pm</math>0.018</u>	0.133	0.140
	MCNP-100	<b>0.394 <math>\pm</math>0.037</b>	<b>0.518 <math>\pm</math>0.040</b>	0.622	0.140
E4 ( $N = 10$ , Neumann)	PINO-20	2.178 $\pm$ 0.368	2.885 $\pm$ 0.368	0.136	0.140
	PINO-100	<u>1.176 <math>\pm</math>0.025</u>	1.805 $\pm$ 0.043	0.627	0.140
	PI-DeepONet	2.587 $\pm$ 0.247	3.111 $\pm$ 0.300	0.433	0.173
	MCNP-20	1.218 $\pm$ 0.016	<u>1.470 <math>\pm</math>0.026</u>	0.133	0.140
	MCNP-100	<b>0.582 <math>\pm</math>0.078</b>	<b>0.671 <math>\pm</math>0.083</b>	0.622	0.140

term to encode the boundary, the boundary conditions in MCNP Solver can be naturally satisfied by choosing the corresponding transition probability. Moreover, the performances of MCNP-20 are generally comparable with PINO-100 while taking only around 21 % of the training time, demonstrating the advantages of neural Monte Carlo loss for learning PDEs in an unsupervised manner.

### 4.3 2D Navier-Stokes Equation

In this experiment, we simulate the vorticity field for 2D incompressible flows in a periodic domain  $\Omega = [0, 1] \times [0, 1]$ , whose vortex equation is given as follows:

$$\begin{aligned} \frac{\partial \omega}{\partial t} &= -(\mathbf{u} \cdot \nabla)\omega + \nu \Delta \omega + f(\mathbf{x}), \quad \mathbf{x} \in \Omega, t \in [0, 10], \\ \omega &= \nabla \times \mathbf{u}, \end{aligned} \quad (21)$$

where  $f(\mathbf{x})$  is the external forcing function,  $\mathbf{u} \in \mathbb{R}^2$  denotes the velocity field, and  $\nu \in \mathbb{R}^+$  represents the viscosity term. The initial vorticity is generated from the Gaussian random field  $\mathcal{N}(0, 7^{3/2}(-\Delta + 49\mathbf{I})^{-2.5})$  with periodic boundaries. In this section, we consider two kinds of external forcing, including the Li forcing  $f_1(\mathbf{x}) \triangleq 0.1 \sin(2\pi(\mathbf{x}_1 + \mathbf{x}_2)) + 0.1 \cos(2\pi(\mathbf{x}_1 + \mathbf{x}_2))$ , which is a classical forcing in the paper of FNO [33], and the Kolmogorov forcing  $f_2(\mathbf{x}) \triangleq 0.1 \cos(8\pi\mathbf{x}_1)$ , which can result in a much wider range of trajectories due to the chaotic [59].

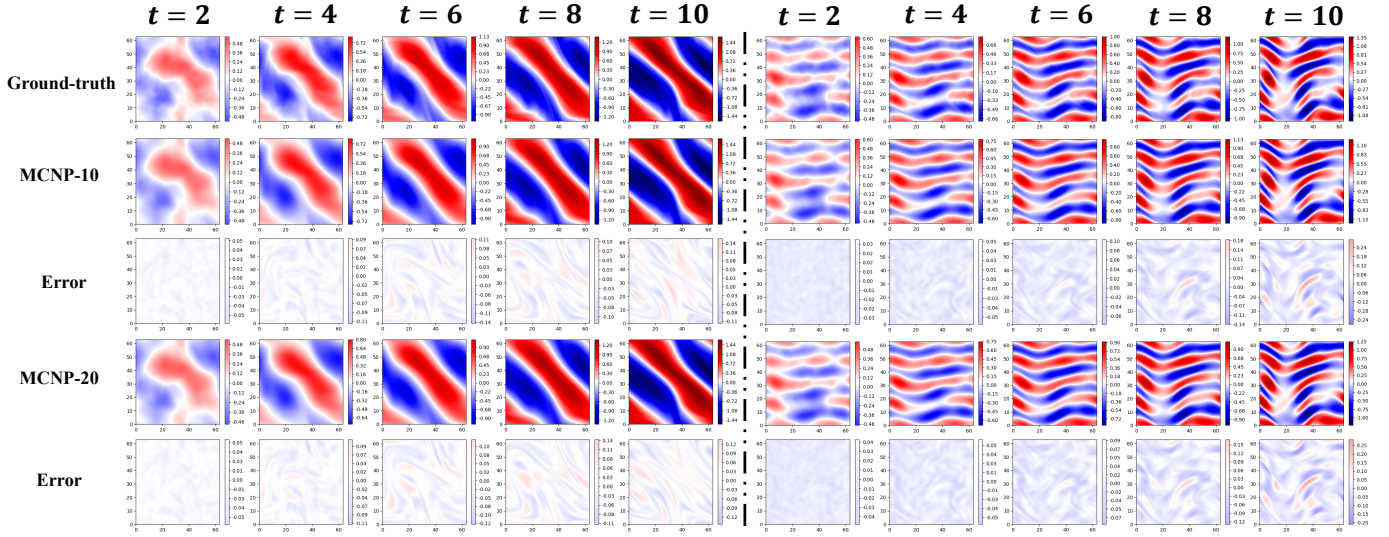


Figure 6: **Simulation of 2D Navier-Stokes equations.** The ground truth vorticity versus the prediction of a learned MCNP Solver for an example in the test set from  $t = 2$  to  $t = 10$ , with the viscosity terms  $\nu = 10^{-5}$ . (Left: the Li forcing; Right: the Kolmogorov forcing.)

Table 3: **2D Navier-Stokes equation with varying  $\nu$  and forcing.** Relative  $\ell_2$  errors ( $E_{\ell_2}$ ), relative  $\ell_\infty$  errors ( $E_{\ell_\infty}$ ) and computational costs for baseline methods and MCNP Solver. The best results are marked in bold, and the second best results are underlined. The training time for MCNP Solvers varies among the four experiments due to the interpolation trick.

Task	Model	$E_{\ell_2}$ (%)	$E_{\ell_\infty}$ (%)	Train Time (H)	Params (M)
E1 ( $\nu = 10^{-4}$ , Li Forcing)	PINO-10	5.502 $\pm$ 0.040	9.002 $\pm$ 0.056	0.232	5.319
	PINO-20	3.971 $\pm$ 0.115	6.819 $\pm$ 0.184	0.413	5.319
	PINO-100	3.366 $\pm$ 0.034	5.908 $\pm$ 0.041	1.919	5.319
	MCNP-10	3.101 $\pm$ 0.043	<u>5.815 <math>\pm</math> 0.075</u>	0.261	5.319
	MCNP-20	<b>2.999 <math>\pm</math> 0.082</b>	<b>5.336 <math>\pm</math> 0.131</b>	0.491	5.319
	E2 ( $\nu = 10^{-5}$ , Li Forcing)	PINO-10	10.617 $\pm$ 0.166	16.799 $\pm$ 0.255	0.232
PINO-20		8.124 $\pm$ 0.261	13.636 $\pm$ 0.351	0.413	5.319
PINO-100		6.439 $\pm$ 0.105	11.123 $\pm$ 0.139	1.919	5.319
MCNP-10		<u>5.825 <math>\pm</math> 0.068</u>	<u>10.452 <math>\pm</math> 0.122</u>	0.260	5.319
MCNP-20		<b>5.776 <math>\pm</math> 0.085</b>	<b>10.137 <math>\pm</math> 0.146</b>	0.531	5.319
E3 ( $\nu = 10^{-4}$ , Kolmogorov Forcing)		PINO-10	6.652 $\pm$ 0.141	8.922 $\pm$ 0.205	0.232
	PINO-20	5.164 $\pm$ 0.138	7.195 $\pm$ 0.196	0.413	5.319
	PINO-100	4.925 $\pm$ 0.037	6.972 $\pm$ 0.042	1.919	5.319
	MCNP-10	<u>4.799 <math>\pm</math> 0.114</u>	<b>6.443 <math>\pm</math> 0.086</b>	0.278	5.319
	MCNP-20	<b>4.609 <math>\pm</math> 0.048</b>	<u>6.488 <math>\pm</math> 0.053</u>	0.518	5.319
	E4 ( $\nu = 10^{-5}$ , Kolmogorov Forcing)	PINO-10	16.342 $\pm$ 0.345	22.497 $\pm$ 0.266	0.232
PINO-20		13.501 $\pm$ 0.446	19.200 $\pm$ 0.748	0.413	5.319
PINO-100		11.874 $\pm$ 0.235	16.973 $\pm$ 0.204	1.919	5.319
MCNP-10		<b>10.161 <math>\pm</math> 0.150</b>	<u>15.053 <math>\pm</math> 0.227</u>	0.252	5.319
MCNP-20		<u>10.829 <math>\pm</math> 0.154</u>	<b>15.764 <math>\pm</math> 0.196</b>	0.528	5.319

### 4.3.1 Experimental Settings

The viscosity term  $\nu$  can be regarded as a measure of the spatiotemporal complexity of the Navier-Stokes equation. As  $\nu$  decreases, the nonlinear term  $(\mathbf{u} \cdot \nabla)\omega$  gradually governs the motion of fluids, increasing the difficulty of simulation. To evaluate the performance of handling different degrees of turbulence, we conduct the experiments with  $\nu$  in  $10^{-4}, 10^{-5}$ , respectively. Therefore, four experimental settings are denoted E1/E2/E3/E4 with  $(f(\mathbf{x}), \nu) = (f_1(\mathbf{x}), 10^{-4}), (f_1(\mathbf{x}), 10^{-5}), (f_2(\mathbf{x}), 10^{-4}), (f_2(\mathbf{x}), 10^{-5})$ , respectively. We divide the domain  $\Omega$  into  $64 \times 64$  uniform grid elements.

### 4.3.2 Baselines

We introduce the baselines conducted on 2D Navier-Stokes equation, including:<sup>1</sup> i). **PINO** [34]: we divide the time interval  $[0, 10]$  into 10/20/100 uniform frames, denoted as PINO-10/20/100, respectively. The loss function is constructed through the pseudo-spectral method due to the periodical boundary conditions. ii). **MCNP Solver**, we divide the time interval into uniform 10/20 frames, which are denoted as MCNP-10/20, respectively.

### 4.3.3 Results

Fig. 6 shows a comparison between the ground truth and predicted  $\omega$  of a learned MCNP Solver from  $t = 2$  to  $t = 10$  with Li and Kolmogorov forcing, respectively. More simulation results of other baseline methods can be seen in the Appendix II. Table 3 presents each method’s performance and computational cost on the 2D Navier-Stokes equations. Compared to PINO, MCNP-10/20 achieved the best and second-best error rate for all tasks and metrics. Unlike PINO, whose performance is highly affected by step size, especially for cases in E2 and E4, MCNP Solver can maintain stability with respect to step size. It is worth mentioning that MCNP-10 outperforms PINO-100 on all metrics while only taking 13.1-14.5 % of the training time. Such an advantage stems from the fact that the Lagrangian method can be better adapted to coarse step size, as discussed in [21, 26].

## 5 Additional Experimental Results

In this section, we conduct several additional numerical experiments to comprehensively compare the scopes and advantages of the proposed MCNP Solver with other widely-used PDE solvers, including the Monte Carlo methods, traditional Eulerian methods and supervised solver learning methods. Furthermore, we conduct ablation studies on MCNP Solver to study the effects of the proposed tricks.

### 5.1 Comparison with Monte Carlo Methods

In this section, we conduct experiments to compare MCNP Solver with Monte Carlo methods on the convection-diffusion equations (E3 and E4) in Section 4.1. The implementation of the Monte Carlo method utilizes the Feynman-Kac law introduced in Section 3.1. We can directly simulate the corresponding SDE due to the linearity of the convection-diffusion equation. We divide the time interval  $[0, 2]$  into 200 uniform frames and sample 200/2000/20000 particles per grid point when conducting the Monte Carlo methods, denoted as MCM/MCM+/MCM++, respectively.

<sup>1</sup>For PI-DeepONets [64], they only conduct experiments on time-independent PDE in 2D situations in their paper.

Table 4: **Compared to the Monte Carlo methods on the 1D convection-diffusion equations with varying  $\kappa$ .** Relative  $\ell_2$  errors ( $E_{\ell_2}$ ), relative  $\ell_\infty$  errors ( $E_{\ell_\infty}$ ) and the inference time for baseline methods and MCNP Solver. The inference time of MCNP Solver reported in this table is the average over E3 and E4.

Methods	E3 ( $\kappa = 0.005, N = 10$ )		E4 ( $\kappa = 0.01, N = 10$ )		Infer Time (S)
	$E_{\ell_2}$ (%)	$E_{\ell_\infty}$ (%)	$E_{\ell_2}$ (%)	$E_{\ell_\infty}$ (%)	
MCM	6.284 $\pm$ 0.058	8.716 $\pm$ 0.081	9.754 $\pm$ 0.402	11.958 $\pm$ 0.439	0.163
MCM+	1.958 $\pm$ 0.046	2.742 $\pm$ 0.053	2.877 $\pm$ 0.084	3.607 $\pm$ 0.122	1.373
MCM++	0.637 $\pm$ 0.037	0.896 $\pm$ 0.049	0.929 $\pm$ 0.104	1.171 $\pm$ 0.112	13.710
MCNP-10	0.160 $\pm$ 0.006	0.239 $\pm$ 0.005	0.182 $\pm$ 0.021	0.233 $\pm$ 0.021	0.005

Table 5: **Compared to the pseudo-spectral methods on 2D Navier-Stokes equation with varying  $\nu$ .** Relative  $\ell_2$  errors ( $E_{\ell_2}$ ), relative  $\ell_\infty$  errors ( $E_{\ell_\infty}$ ) and the inference time for baseline methods and MCNP Solver. We unitize NAN to represent the result whose relative error is larger than 200 %.

Methods	E1 ( $\nu = 10^{-4}$ )		E2 ( $\nu = 10^{-5}$ )		Infer Time (S)
	$E_{\ell_2}$ (%)	$E_{\ell_\infty}$ (%)	$E_{\ell_2}$ (%)	$E_{\ell_\infty}$ (%)	
PSM-500	NAN	NAN	NAN	NAN	0.350
PSM-1000	0.163	0.394	NAN	NAN	0.629
PSM-2000	0.115	0.231	1.653	6.562	1.220
MCNP-20	2.999 $\pm$ 0.082	5.336 $\pm$ 0.131	5.776 $\pm$ 0.085	10.137 $\pm$ 0.146	0.008

Table 4 presents a comparison between MCNP-10 and corresponding Monte Carlo methods. The performances of Monte Carlo methods are limited by the number of particles, especially for large heat transfer rate  $\kappa$ . Sampling a large number of particles can reduce errors, but it also brings severe computation issues, such as GPU memory and inference time. However, the MCNP Solver can approximate the mathematical expectation in Eq. 7 via the PDF of neighbour grid points rather than sampling amounts of particles, as we introduced in Section 3.3.2.

## 5.2 Comparison with Traditional Eulerian Solver

In this section, we conduct experiments to compare MCNP Solver with traditional pseudo-spectral methods on the Navier-Stokes equations (E1 and E2) in Section 4.3, which is one kind of state-of-the-art numerical methods on periodical PDEs. The implementation of the pseudo-spectral method is in line with [33], which utilizes the Crank–Nicolson scheme for the temporal revolution. We divide the time interval  $[0, 10]$  into 500/1000/2000 uniform frames and denote them as PSM-500/1000/2000, respectively.

Table 5 presents a comparison between MCNP-20 and PSM-500/1000/2000. The pseudo-spectral methods must refine the time interval to obtain meaningful simulation results, especially for cases with a low viscosity term  $\nu$ . PSM-2000 achieves the lowest error rate on all tasks but requires 150 times more inference time than neural PDE solvers. In summary, the precision of the MCNP Solver cannot outperform the numerical solvers when ignoring the inference time, which is also a major drawback for other existing deep learning-based methods [13, 60]. However, due to its zero-shot inference nature, the neural PDE solver has a unique application scenario. As

Table 6: **Compared to the FNO on 2D Navier-Stokes equation with varying  $\nu$ .** Relative  $\ell_2$  errors ( $E_{\ell_2}$ ), relative  $\ell_\infty$  errors ( $E_{\ell_\infty}$ ) and the training costs for baseline methods and MCNP Solver. The training time of MCNP Solver reported in this table is the average over E1 and E2.

Methods	E1 ( $\nu = 10^{-4}$ )		E2 ( $\nu = 10^{-5}$ )		Time (H)		
	$E_{\ell_2}$ (%)	$E_{\ell_\infty}$ (%)	$E_{\ell_2}$ (%)	$E_{\ell_\infty}$ (%)	Data	Train	Total
FNO	4.754 $\pm$ 0.139	8.934 $\pm$ 0.248	8.003 $\pm$ 0.161	15.184 $\pm$ 0.239	0.346	0.207	0.553
FNO+	3.460 $\pm$ 0.163	6.630 $\pm$ 0.358	6.115 $\pm$ 0.085	11.743 $\pm$ 0.143	0.692	0.207	0.899
FNO++	2.619 $\pm$ 0.124	4.906 $\pm$ 0.195	4.640 $\pm$ 0.032	8.839 $\pm$ 0.148	1.384	0.207	1.591
MCNP-10	3.101 $\pm$ 0.043	5.815 $\pm$ 0.075	5.825 $\pm$ 0.068	10.452 $\pm$ 0.122	0	0.261	0.261
MCNP-20	2.999 $\pm$ 0.082	5.336 $\pm$ 0.131	5.776 $\pm$ 0.085	10.137 $\pm$ 0.146	0	0.511	0.511

Table 7: **Ablation Studies of each method component in MCNP Solver.** Relative error (%) and training time for each method on the Navier-Stokes equation tasks with  $\nu = 10^{-4}$  (E1) and  $\nu = 10^{-5}$  (E2). The training time of each method reported in this table is the average over E1 and E2.

Methods	E1 ( $\nu = 10^{-4}$ )		E2 ( $\nu = 10^{-5}$ )		Train Time (H)
	$E_{\ell_2}$ (%)	$E_{\ell_\infty}$ (%)	$E_{\ell_2}$ (%)	$E_{\ell_\infty}$ (%)	
MCNP-H-10	11.572 $\pm$ 0.009	19.482 $\pm$ 0.013	13.374 $\pm$ 0.055	23.280 $\pm$ 0.076	0.253
MCNP-I-10	3.168 $\pm$ 0.026	5.931 $\pm$ 0.048	61.719 $\pm$ 3.475	78.465 $\pm$ 9.320	0.242
MCNP-10	3.101 $\pm$ 0.043	5.815 $\pm$ 0.075	5.825 $\pm$ 0.068	10.452 $\pm$ 0.122	0.261
MCNP-H-20	7.104 $\pm$ 0.048	12.403 $\pm$ 0.080	9.249 $\pm$ 0.041	16.613 $\pm$ 0.101	0.509
MCNP-I-20	8.970 $\pm$ 0.025	15.138 $\pm$ 0.026	69.067 $\pm$ 5.975	72.800 $\pm$ 4.340	0.408
MCNP-20	2.999 $\pm$ 0.082	5.336 $\pm$ 0.131	5.776 $\pm$ 0.085	10.137 $\pm$ 0.146	0.511

discussed in [60], *AI-based methods lack precision compared to classical methods while achieving reasonable accuracy and offering great potential for efficient parameter studies.*

### 5.3 Comparison with Supervised Solver Learning

In this section, we conduct experiments to compare MCNP Solver with supervised neural operator learning methods FNO [33] on the Navier-Stokes equations (E1 and E2) in Section 4.3. To evaluate the performance of FNO with the amounts of datasets, we utilize 500/1000/2000 PDE trajectories to train FNO and denote the corresponding methods as FNO/FNO+/FNO++, respectively.

Table 6 presents a comparison between MCNP-10/20 and three versions of FNO. Compared to the supervised methods, which use pre-simulated fixed data for training, MCNP Solver can sample new initial fields per epoch, thereby increasing the diversity of training data. As a result, MCNP-10/20 can outperform FNO and FNO+. With the increase of training data, FNO++ achieves better results. This is because the training data is generated from high-precision numerical methods, while the unsupervised methods construct the loss function with low spatiotemporal resolution. However, as a trade-off, FNO++ spends 211-510 % more total time compared to MCNP-20/10.

## 5.4 Ablation Studies

In this section, we conduct several ablation studies on the MCNP Solver applied to the Navier-Stokes equation (E1 and E2). Our goal is to demonstrate the individual contributions of different method components. MCNP-H replaces Heun’s method (Section 3.3.1) with the traditional Euler method when simulating the SDEs. MCNP-I represents the MCNP Solver without the interpolation trick introduced in Section 3.3.3.

Table 7 reports the results and training costs. Compared to MCNP Solver with MCNP-H, the results show that using Heun’s method to simulate the SDEs significantly improves the accuracy of MCNP Solver, while incurring only minimal additional computational cost, especially for MCNP-10. Compared to MCNP Solver with MCNP-I, the interpolation trick plays a crucial role in E2 when  $\nu = 10^{-5}$ . As discussed in Section 3.3.3, extremely low diffusion rates can lead to very short-distance diffusion effects, resulting in  $\sum_i p_t(\xi_{p,t}^{d,i})\delta \ll 1$ . Therefore, interpolating the original vorticity field becomes essential to ensure that the PDF of grid points satisfies normalization conditions in Eq. 17. Similarly, the interpolation trick can reduce more relative error for MCNP-20 than MCNP-10 in E1 because fine step size can also introduce localized random walks per step.

## 6 Conclusion and Discussion

**Conclusion** In this paper, we propose the MCNP Solver, which leverages the Feynman-Kac formula to train neural PDE solvers in an unsupervised manner. Numerical analyses demonstrate the MCNP Solver’s ability to adapt to complex spatiotemporal variations and coarse step size on convection-diffusion, Allen-Cahn and Navier-Stokes equations.

**Limitations** This paper has several limitations: (1) Some PDEs are not suitable for the Feynman-Kac formula and therefore do not fall within the scope of the MCNP Solver, such as third or higher-order PDEs (involving high-order operators like  $u_{xxx}$ ). (2) The accuracy of the MCNP Solver cannot outperform traditional numerical solvers when disregarding inference time, which is also a major drawback for other existing neural solvers [13, 60], as we discussed in Section 3.3.2.

**Future Work** We suggest several directions for future research: (1) Extend the proposed MCNP Solver to broader scenarios, such as high-dimensional PDEs and optimal control problems; (2) Utilize techniques from out-of-distribution generalization [57] to improve the generalization ability of MCNP Solver.

## Appendix I: Implementation Details

### I.1: Baselines

In this paper, we adopt Pytorch [46] to implement MCNP Solver, FNO, and PINO, and JAX [3] for PI-DeepONet, respectively. Here, we introduce two different unsupervised methods as follows.

## PI-DeepONet [64]

PI-DeepONet utilizes the PDE residuals to train DeepONets in an unsupervised way. The loss function in PI-DeepONet can be formulated as follows:

$$\begin{aligned}\mathcal{L}_{\text{PI-DeepONet}} &= \lambda_1 \mathcal{L}_{\text{initial}} + \lambda_2 \mathcal{L}_{\text{boundary}} + \mathcal{L}_{\text{physics}}, \\ \text{where } \mathcal{L}_{\text{initial}} &= \text{RMSE}[\mathcal{G}_\theta(u_0^b, t=0)(\mathbf{x}_p) - \mathcal{G}(u_0^b, t=0)(\mathbf{x}_p)], \\ \mathcal{L}_{\text{boundary}} &= \text{RMSE}[\mathcal{B}(\mathcal{G}_\theta, \mathbf{x}, t)], \\ \mathcal{L}_{\text{physics}} &= \text{RMSE}[\mathcal{R}(\mathcal{G}_\theta(u_0^b, t)(\mathbf{x}_p), \mathbf{x}_p, t)],\end{aligned}\tag{22}$$

where RMSE represents the rooted mean square error,  $\mathcal{G}_\theta$  represents a neural operator,  $\mathcal{G}$  and  $\mathcal{R}$  denote the ground truth and the residual of the PDE operator, respectively. As shown in Eq. 22,  $\mathcal{L}_{\text{initial}}$ ,  $\mathcal{L}_{\text{boundary}}$  and  $\mathcal{L}_{\text{physics}}$  enforce  $\mathcal{G}_\theta$  to satisfy the initial conditions, boundary conditions and the PDE constraints, respectively. Like PINNs [50], the PDE residuals in Eq. 22 are calculated via the auto-differentiation.

## PINO [34]

PINO utilizes the pseudo-spectral or finite difference methods to construct the loss function between  $\mathcal{G}_\theta(u_t^b)$  and  $\mathcal{G}_\theta(u_{t+\Delta t}^b)$ . PINO utilized the FNO [29] as the backbone network. The loss function in PINO can be formulated as follows:

$$\begin{aligned}\mathcal{L}_{\text{PINO}} &= \lambda \mathcal{L}_{\text{boundary}} + \mathcal{L}_{\text{physics}}, \\ \text{where } \mathcal{L}_{\text{boundary}} &= \text{RMSE}[\mathcal{B}(\mathcal{G}_\theta, \mathbf{x}, t)], \\ \mathcal{L}_{\text{physics}} &= \sum_{t=0}^{T-\Delta t} \text{RMSE}[\mathcal{G}_\theta(u_0^b, t + \Delta t)(\mathbf{x}_p) - \mathcal{P}(\mathcal{G}_\theta, \mathbf{x}_p, t)],\end{aligned}\tag{23}$$

where  $\mathcal{B}$  denotes the constraints on the boundary conditions, and  $\mathcal{P}$  denotes the update regime of numerical PDE solvers.

## I.2: 1D Convection-Diffusion Equation

### Data

The initial states  $u(x, 0)$  are generated from the functional space  $\mathcal{F}_N \triangleq \{\sum_{n=1}^N a_n \sin(2\pi nx) : a_n \sim \mathbb{U}(0, 1)\}$ , where  $\mathbb{U}(0, 1)$  denotes the uniform distribution over  $(0, 1)$ , and  $N$  represents the maximum frequency of the functional space. We generate the ground truth with the pseudo-spectral methods with the Runge-Kutta 2 regime. All PDE instances are generated on the spatial grid 1024, then down-sampled to 64. The step size is fixed as  $10^{-5}$ . We generate 200 test data with seed 1 and 200 validation data with seed 2.

### Hyperparameters

The PINO and MCNP Solver use the 1D FNO as the backbone models. We fix the number of layers and widths as 4 and 32, respectively. We choose the best *mode* in  $\{12, 16, 20\}$  for FNO, respectively. For PINO and MCNP Solver, we utilize Adam to optimize the neural network for 10000 epochs with an initial learning rate  $lr$  and decay the learning rate by a factor of 0.5 every 1000 epochs. The batch size is fixed as 200. The learning rate is chosen from the set  $\{0.02, 0.01, 0.005, 0.001\}$ . Because the pseudo-spectral methods can naturally stratify the boundary conditions, we fix  $\lambda$  as 0 in this section. For PI-DeepONet, we choose the network

structure in line with the 1D case in [64] and extend the training iterations to 50000 to ensure the convergence of the model. Moreover, we search the hyperparameters  $\lambda_1$ ,  $\lambda_2$  and the width of the neural networks in  $\{1, 5, 10\}$ ,  $\{1, 5, 10, 25, 50\}$  and  $\{80, 100, 120\}$ , respectively. All hyperparameters are chosen via the validation set with seed 0.

### I.3: 1D Allen-Cahn Equation

#### Data

The initial states  $u(x, 0)$  are generated from the functional space  $\mathcal{F}_N \triangleq \{\sum_{n=1}^N a_n \sin(2\pi nx) : a_n \sim \mathbb{U}(0, 1)\}$ , where  $\mathbb{U}(0, 1)$  denotes the uniform distribution over  $(0, 1)$ , and  $N$  represents the maximum frequency of the functional space. We generate the ground truth with the Python package ‘py-pde’ [70]. All PDE instances are generated on the spatial grid 1024, then down-sampled to 65. The step size is fixed as  $10^{-6}$ . We generate 200 test data with seed 1 and 200 validation data with seed 2.

#### Hyperparameters

The PINO and MCNP Solver use the 1D FNO as the backbone models. We fix the number of layers and widths as 4 and 32, respectively. We choose the best *mode* in  $\{12, 16, 20\}$  for FNO, respectively. For PINO and MCNP Solver, we utilize Adam to optimize the neural network for 20000 epochs with an initial learning rate  $lr$  and decay the learning rate by a factor of 0.5 every 2000 epochs. The batch size is fixed as 200. The learning rate is chosen from the set  $\{0.02, 0.01, 0.005, 0.001\}$ . The hyperparameter  $\lambda$  in the PINO loss is chosen from the set  $\{1, 2, 5, 10, 25, 50\}$ . For PI-DeepONet, we choose the network structure in line with the 1D case in [64] and extend the training iterations to 200000 to ensure the convergence of the model. Moreover, we search the hyperparameters  $\lambda_1$ ,  $\lambda_2$  and the width of the neural networks in  $\{1, 5, 10\}$ ,  $\{1, 5, 10, 25, 50\}$  and  $\{80, 100, 120\}$ , respectively. All hyperparameters are chosen via the validation set with seed 0.

### I.4: 2D Navier-Stokes Equation

#### Data

We utilize the pseudo-spectral methods to generate the ground truth test data with the step size of  $10^{-4}$  for the Crank–Nicolson scheme. Furthermore, all PDE instances are generated on the grid  $256 \times 256$ , then down-sampled to  $64 \times 64$ , which is in line with the setting in [29]. We generate 200 test data with seed 0, 200 validation data with seed 1 and 2000 training data with seed 2.

#### Hyperparameters

The PINO and MCNP Solver use the 2D FNO as the backbone models. We fix the number of layers and widths as 4 and 36, respectively. We choose the best *mode* in  $\{12, 16, 20\}$  for FNO, respectively. For PINO and MCNP Solver, we utilize Adam to optimize the neural network for 20000 epochs with an initial learning rate of  $lr$  and decay the learning rate by a factor of 0.8 every 2000 epochs. The batch size is fixed as 10. The learning rate  $lr$  is chosen from the set  $\{0.02, 0.01, 0.005, 0.001\}$ . Because the pseudo-spectral methods can naturally stratify the boundary conditions, we fix the  $\lambda$  as 0 in this section. For FNO, we find that a cosine annealing schedule can obtain the best result when training with the supervised regime. Therefore, we

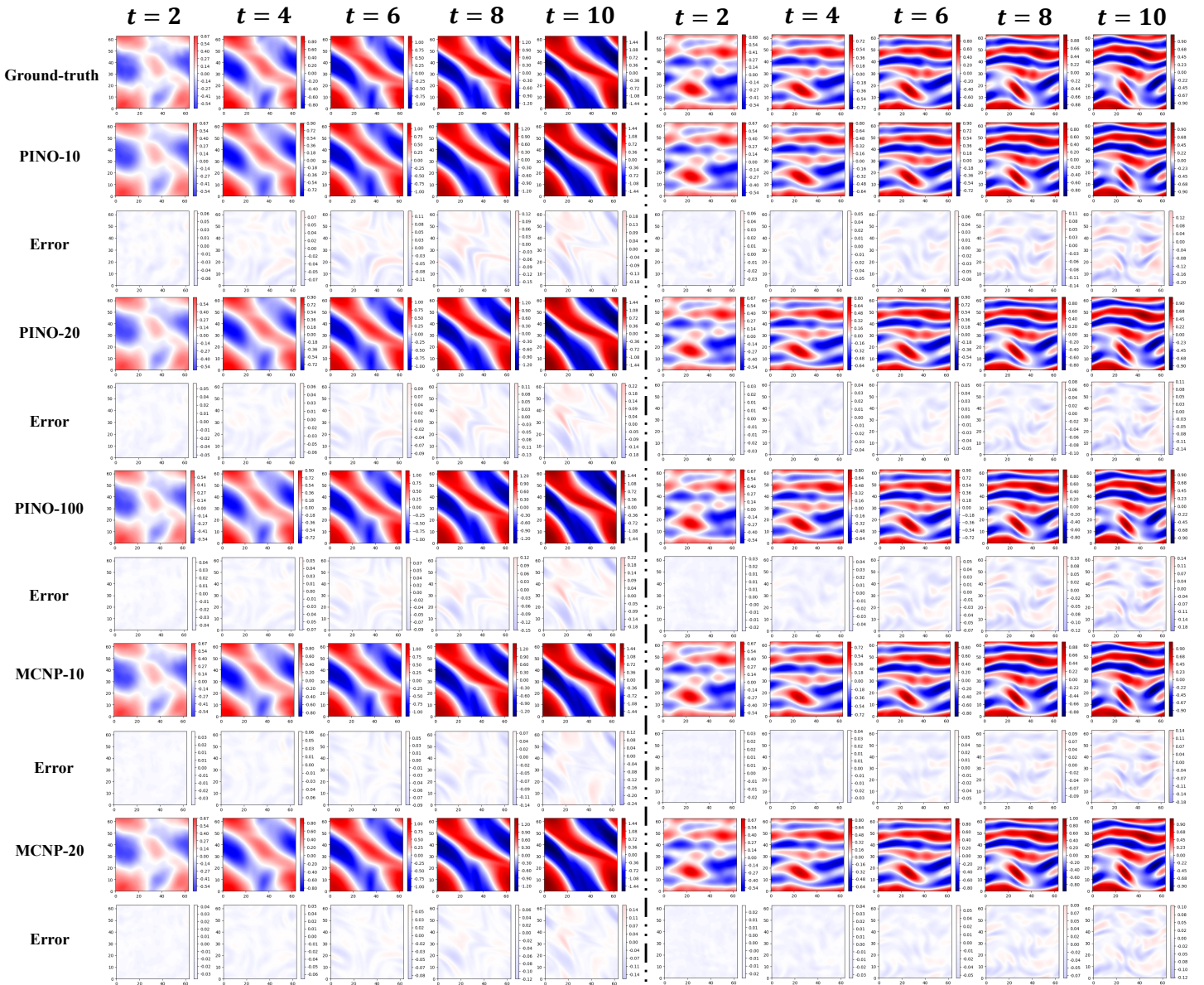


Figure 7: **Simulation of 2D Navier-Stokes equations.** The ground truth vorticity versus the prediction of learned neural PDE solvers for an example in the test set from  $t = 2$  to  $t = 10$ , with the viscosity terms  $\nu = 10^{-4}$ . (Left: the Li forcing; Right: the Kolmogorov forcing.)

utilize Adam to optimize the neural network for 400/200/100 epochs with the initial learning rate of  $lr$  for FNO/FNO+/FNO++, respectively. The learning rate  $lr$  is chosen from the set  $\{0.02, 0.01, 0.005, 0.001\}$ . All hyperparameters are chosen via the validation set with seed 0.

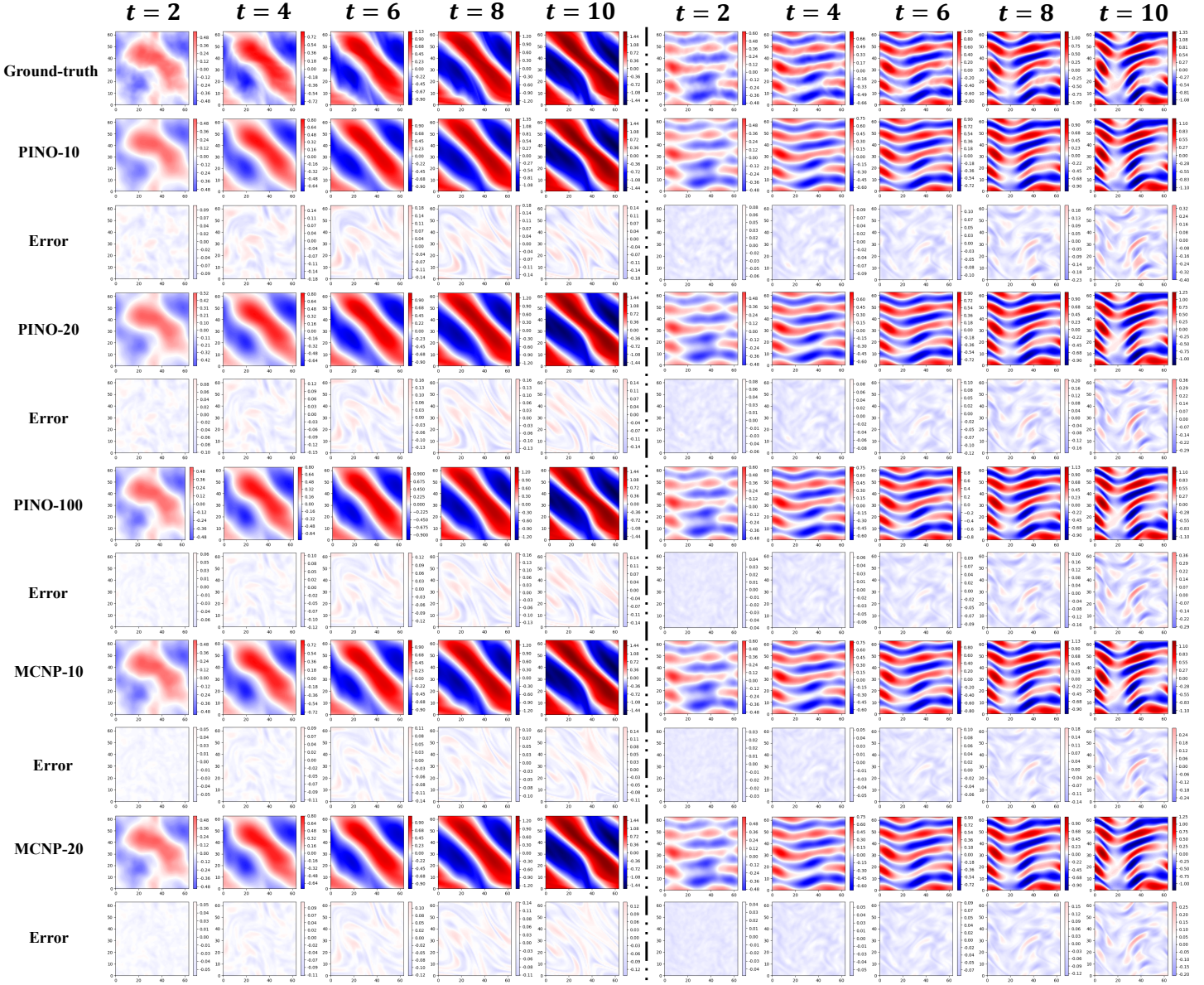


Figure 8: **Simulation of 2D Navier-Stokes equations.** The ground truth vorticity versus the prediction of learned neural PDE solvers for an example in the test set from  $t = 2$  to  $t = 10$ , with the viscosity terms  $\nu = 10^{-5}$ . (Left: the Li forcing; Right: the Kolmogorov forcing.)

## Appendix II: Additional Simulation Results

In this section, we present a comparison between the ground truth and the predicted vorticity fields  $\omega$  of all unsupervised methods from  $t = 2$  to  $t = 10$  with Li and Kolmogorov forcing, respectively (Fig. 7 and 8). According to Fig. 7 and 8, all methods can capture the shape of the fluid, while MCNP Solver can most accurately capture the details and minimize the error magnitude at the intersection of the vorticity direction.

## References

- [1] W. F. Bauer. The monte carlo method. Journal of the Society for Industrial and Applied Mathematics, 6(4):438–451, 1958.
- [2] Deniz A Bezgin, Steffen J Schmidt, and Nikolaus A Adams. A data-driven physics-informed finite-volume scheme for nonclassical undercompressive shocks. Journal of Computational Physics, 437:110324, 2021.
- [3] James Bradbury, Roy Frostig, Peter Hawkins, Matthew James Johnson, Chris Leary, Dougal Maclaurin, George Necula, Adam Paszke, Jake VanderPlas, Skye Wanderman-Milne, and Qiao Zhang. JAX: composable transformations of Python+NumPy programs, 2018.
- [4] Johannes Brandstetter, Daniel E. Worrall, and Max Welling. Message passing neural PDE solvers. In International Conference on Learning Representations, 2022.
- [5] Shuhao Cao. Choose a transformer: Fourier or galerkin. In A. Beygelzimer, Y. Dauphin, P. Liang, and J. Wortman Vaughan, editors, Advances in Neural Information Processing Systems, 2021.
- [6] Zhao Chen, Yang Liu, and Hao Sun. Physics-informed learning of governing equations from scarce data. Nature communications, 12(1):1–13, 2021.
- [7] Alexandre Joel Chorin and Ole H Hald. Stochastic tools in mathematics and science, volume 1. Springer, 2009.
- [8] Georges-Henri Cottet, Petros D Koumoutsakos, et al. Vortex methods: theory and practice, volume 8. Cambridge university press Cambridge, 2000.
- [9] Robert Dalang, Carl Mueller, and Roger Tribe. A feynman-kac-type formula for the deterministic and stochastic wave equations and other pde’s. Transactions of the American Mathematical Society, 360(9):4681–4703, 2008.
- [10] Francis X Giraldo and Beny Neta. A comparison of a family of eulerian and semi-lagrangian finite element methods for the advection-diffusion equation. WIT Transactions on The Built Environment, 30, 1997.
- [11] Raghav Gnanasambandam, Bo Shen, Jihoon Chung, Xubo Yue, and Zhenyu Kong. Self-scalable tanh (stan): Multi-scale solutions for physics-informed neural networks. IEEE Transactions on Pattern Analysis and Machine Intelligence, 2023.
- [12] Somdatta Goswami, Aniruddha Bora, Yue Yu, and George Em Karniadakis. Physics-informed neural operators. arXiv preprint arXiv:2207.05748, 2022.
- [13] Tamara G. Grossmann, Urszula Julia Komorowska, Jonas Latz, and Carola-Bibiane Schönlieb. Can physics-informed neural networks beat the finite element method?, 2023.
- [14] Ling Guo, Hao Wu, Xiaochen Yu, and Tao Zhou. Monte carlo fpinns: Deep learning method for forward and inverse problems involving high dimensional fractional partial differential equations. Computer Methods in Applied Mechanics and Engineering, 400:115523, 2022.
- [15] Patrik Simon Hadorn. Shift-deeponet: Extending deep operator networks for discontinuous output functions. ETH Zurich, Seminar for Applied Mathematics, 2022.
- [16] Jiequn Han, Arnulf Jentzen, and Weinan E. Solving high-dimensional partial differential equations using deep learning. Proceedings of the National Academy of Sciences, 115(34):8505–8510, 2018.
- [17] Jihun Han, Mihai Nica, and Adam R Stinchcombe. A derivative-free method for solving elliptic partial differential equations with deep neural networks. Journal of Computational Physics, 419:109672, 2020.

- [18] Pierre Henry-Labordere, Xiaolu Tan, and Nizar Touzi. A numerical algorithm for a class of bsdes via the branching process. *Stochastic Processes and their Applications*, 124(2):1112–1140, 2014.
- [19] Jan Hermann, Zeno Schätzle, and Frank Noé. Deep-neural-network solution of the electronic schrödinger equation. *Nature Chemistry*, 12(10):891–897, 2020.
- [20] Xiang Huang, Zhanhong Ye, Hongsheng Liu, Shi Bei Ji, Zidong Wang, Kang Yang, Yang Li, Min Wang, Haotian CHU, Fan Yu, Bei Hua, Lei Chen, and Bin Dong. Meta-auto-decoder for solving parametric partial differential equations. In Alice H. Oh, Alekh Agarwal, Danielle Belgrave, and Kyunghyun Cho, editors, *Advances in Neural Information Processing Systems*, 2022.
- [21] Vladimir Irisov and Alexander Voronovich. Numerical simulation of wave breaking. *Journal of physical oceanography*, 41(2):346–364, 2011.
- [22] Xiaowei Jin, Shengze Cai, Hui Li, and George Em Karniadakis. Nsfnets (navier-stokes flow nets): Physics-informed neural networks for the incompressible navier-stokes equations. *Journal of Computational Physics*, 426:109951, 2021.
- [23] Matthias Karlbauer, Timothy Praditia, Sebastian Otte, Sergey Oladyshkin, Wolfgang Nowak, and Martin V Butz. Composing partial differential equations with physics-aware neural networks. In *International Conference on Machine Learning*, pages 10773–10801. PMLR, 2022.
- [24] George Em Karniadakis, Ioannis G Kevrekidis, Lu Lu, Paris Perdikaris, Sifan Wang, and Liu Yang. Physics-informed machine learning. *Nature Reviews Physics*, 3(6):422–440, 2021.
- [25] Nikola Kovachki, Zongyi Li, Burigede Liu, Kamyar Azizzadenesheli, Kaushik Bhattacharya, Andrew Stuart, and Anima Anandkumar. Neural operator: Learning maps between function spaces with applications to pdes. *Journal of Machine Learning Research*, 24(89):1–97, 2023.
- [26] Peter R Kramer. A review of some monte carlo simulation methods for turbulent systems. 2001.
- [27] Aditi Krishnapriyan, Amir Gholami, Shandian Zhe, Robert Kirby, and Michael W Mahoney. Characterizing possible failure modes in physics-informed neural networks. *Advances in Neural Information Processing Systems*, 34:26548–26560, 2021.
- [28] Jae Yong Lee, SungWoong CHO, and Hyung Ju Hwang. HyperdeepONet: learning operator with complex target function space using the limited resources via hypernetwork. In *The Eleventh International Conference on Learning Representations*, 2023.
- [29] Hong Li, Qilong Zhai, and Jeff ZY Chen. Neural-network-based multistate solver for a static schrödinger equation. *Physical Review A*, 103(3):032405, 2021.
- [30] Zijie Li, Kazem Meidani, and Amir Barati Farimani. Transformer for partial differential equations’ operator learning. *arXiv preprint arXiv:2205.13671*, 2022.
- [31] Zongyi Li, Daniel Zhengyu Huang, Burigede Liu, and Anima Anandkumar. Fourier neural operator with learned deformations for pdes on general geometries. *arXiv preprint arXiv:2207.05209*, 2022.
- [32] Zongyi Li, Nikola Kovachki, Kamyar Azizzadenesheli, Burigede Liu, Kaushik Bhattacharya, Andrew Stuart, and Anima Anandkumar. Neural operator: Graph kernel network for partial differential equations. *arXiv preprint arXiv:2003.03485*, 2020.
- [33] Zongyi Li, Nikola Borislavov Kovachki, Kamyar Azizzadenesheli, Burigede Liu, Kaushik Bhattacharya, Andrew M. Stuart, and Anima Anandkumar. Fourier neural operator for parametric partial differential equations. In *9th International Conference on Learning Representations, ICLR 2021, Virtual Event, Austria, May 3-7, 2021*. OpenReview.net, 2021.

- [34] Zongyi Li, Hongkai Zheng, Nikola Kovachki, David Jin, Haoxuan Chen, Burigede Liu, Kamyar Azizzadenesheli, and Anima Anandkumar. Physics-informed neural operator for learning partial differential equations. arXiv preprint arXiv:2111.03794, 2021.
- [35] Lu Lu, Pengzhan Jin, Guofei Pang, Zhongqiang Zhang, and George Em Karniadakis. Learning nonlinear operators via deepnet based on the universal approximation theorem of operators. Nature Machine Intelligence, 3(3):218–229, 2021.
- [36] Sylvain Maire and Etienne Tanré. Monte carlo approximations of the neumann problem. In Monte Carlo Methods Appl., 2012.
- [37] Xuerong Mao. Stochastic differential equations and applications. Elsevier, 2007.
- [38] Nils Margenber, Dirk Hartmann, Christian Lessig, and Thomas Richter. A neural network multi-grid solver for the navier-stokes equations. Journal of Computational Physics, 460:110983, 2022.
- [39] Revanth Mathey and Susanta Ghosh. A novel sequential method to train physics informed neural networks for allen cahn and cahn hilliard equations. Computer Methods in Applied Mechanics and Engineering, 390:114474, 2022.
- [40] Chloé Mimeau and Iraj Mortazavi. A review of vortex methods and their applications: From creation to recent advances. Fluids, 6(2):68, 2021.
- [41] Sebastian K Mitusch, Simon W Funke, and Miroslav Kuchta. Hybrid fem-nn models: Combining artificial neural networks with the finite element method. Journal of Computational Physics, 446:110651, 2021.
- [42] Nikolas Nüsken and Lorenz Richter. Interpolating between bsdes and pinns—deep learning for elliptic and parabolic boundary value problems. arXiv preprint arXiv:2112.03749, 2021.
- [43] Panos Pantidis and Mostafa E Mobasher. Integrated finite element neural network (i-fenn) for non-local continuum damage mechanics. Computer Methods in Applied Mechanics and Engineering, 404:115766, 2023.
- [44] Etienne Pardoux and Shige Peng. Backward stochastic differential equations and quasilinear parabolic partial differential equations. In Stochastic partial differential equations and their applications, pages 200–217. Springer, 1992.
- [45] Etienne Pardoux and Shanjian Tang. Forward-backward stochastic differential equations and quasilinear parabolic pdes. Probability Theory and Related Fields, 114(2):123–150, 1999.
- [46] Adam Paszke, Sam Gross, Francisco Massa, Adam Lerer, James Bradbury, Gregory Chanan, Trevor Killeen, Zeming Lin, Natalia Gimelshein, Luca Antiga, et al. Pytorch: An imperative style, high-performance deep learning library. Advances in neural information processing systems, 32, 2019.
- [47] Huyen Pham. Feynman-kac representation of fully nonlinear pdes and applications. Acta Mathematica Vietnamica, 40:255–269, 2015.
- [48] Zhongmin Qian, Endre Süli, and Yihuang Zhang. Random vortex dynamics via functional stochastic differential equations. Proceedings of the Royal Society A, 478(2266):20220030, 2022.
- [49] Md Ashiqur Rahman, Zachary E Ross, and Kamyar Azizzadenesheli. U-NO: U-shaped neural operators. Transactions on Machine Learning Research, 2023.
- [50] Maziar Raissi, Paris Perdikaris, and George E Karniadakis. Physics-informed neural networks: A deep learning framework for solving forward and inverse problems involving nonlinear partial differential equations. Journal of Computational physics, 378:686–707, 2019.

- [51] Maziar Raissi, Alireza Yazdani, and George Em Karniadakis. Hidden fluid mechanics: Learning velocity and pressure fields from flow visualizations. *Science*, 367(6481):1026–1030, 2020.
- [52] Lorenz Richter and Julius Berner. Robust sde-based variational formulations for solving linear pdes via deep learning. In *International Conference on Machine Learning*, pages 18649–18666. PMLR, 2022.
- [53] Lorenz Richter, Leon Sallandt, and Nikolas Nüsken. Solving high-dimensional parabolic pdes using the tensor train format. In *International Conference on Machine Learning*, pages 8998–9009. PMLR, 2021.
- [54] Emanuele Rossi, Andrea Colagrossi, and Giorgio Graziani. Numerical simulation of 2d-vorticity dynamics using particle methods. *Computers & Mathematics with Applications*, 69(12):1484–1503, 2015.
- [55] Rohan Sawhney, Dario Seyb, Wojciech Jarosz, and Keenan Crane. Grid-free monte carlo for pdes with spatially varying coefficients. *ACM Transactions on Graphics (TOG)*, 41(4):1–17, 2022.
- [56] Jacob H Seidman, Georgios Kissas, Paris Perdikaris, and George J. Pappas. NOMAD: Nonlinear manifold decoders for operator learning. In Alice H. Oh, Alekh Agarwal, Danielle Belgrave, and Kyunghyun Cho, editors, *Advances in Neural Information Processing Systems*, 2022.
- [57] Zheyang Shen, Jiashuo Liu, Yue He, Xingxuan Zhang, Renzhe Xu, Han Yu, and Peng Cui. Towards out-of-distribution generalization: A survey. *arXiv preprint arXiv:2108.13624*, 2021.
- [58] Wenlei Shi, Xinquan Huang, Xiaotian Gao, Xinran Wei, Jia Zhang, Jiang Bian, Mao Yang, and Tie-Yan Liu. Lordnet: Learning to solve parametric partial differential equations without simulated data. *arXiv preprint arXiv:2206.09418*, 2022.
- [59] Nejib Smaoui, Alaa El-Kadri, and Mohamed Zribi. On the control of the 2d navier–stokes equations with kolmogorov forcing. *Complexity*, 2021:1–18, 2021.
- [60] Derick Nganyu Tanyu, Jianfeng Ning, Tom Freudenberg, Nick Heilenkötter, Andreas Rademacher, Uwe Iben, and Peter Maass. Deep learning methods for partial differential equations and related parameter identification problems, 2022.
- [61] Alasdair Tran, Alexander Mathews, Lexing Xie, and Cheng Soon Ong. Factorized fourier neural operators. In *The Eleventh International Conference on Learning Representations*, 2023.
- [62] Simone Venturi and Tiernan Casey. Svd perspectives for augmenting deepoNet flexibility and interpretability. *Computer Methods in Applied Mechanics and Engineering*, 403:115718, 2023.
- [63] J. Vom Scheidt. Kloeden, p. e.; platen, e., numerical solution of stochastic differential equations. berlin etc., springer-verlag 1992. xxxvi, 632 pp., 85 figs., dm 118,00. isbn 3-540-54062-8 (applications of mathematics 23). *ZAMM - Journal of Applied Mathematics and Mechanics / Zeitschrift für Angewandte Mathematik und Mechanik*, 74(8):332–332, 1994.
- [64] Sifan Wang, Hanwen Wang, and Paris Perdikaris. Learning the solution operator of parametric partial differential equations with physics-informed deepoNets. *Science advances*, 7(40):eabi8605, 2021.
- [65] Sifan Wang, Xinling Yu, and Paris Perdikaris. When and why pinns fail to train: A neural tangent kernel perspective. *Journal of Computational Physics*, 449:110768, 2022.
- [66] Yizheng Wang, Jia Sun, Wei Li, Zaiyuan Lu, and Yinghua Liu. Cenn: Conservative energy method based on neural networks with subdomains for solving variational problems involving heterogeneous and complex geometries. *Computer Methods in Applied Mechanics and Engineering*, 400:115491, 2022.

- [67] Li-Ming Yang. Kinetic theory of diffusion in gases and liquids. i. diffusion and the brownian motion. Proceedings of the Royal Society of London. Series A, Mathematical and Physical Sciences, pages 94–116, 1949.
- [68] Rui Zhang, Peiyan Hu, Qi Meng, Yue Wang, Rongchan Zhu, Bingguang Chen, Zhi-Ming Ma, and Tie-Yan Liu. Drvn (deep random vortex network): A new physics-informed machine learning method for simulating and inferring incompressible fluid flows. Physics of Fluids, 34(10):107112, 2022.
- [69] Qingqing Zhao, David B. Lindell, and Gordon Wetzstein. Learning to solve pde-constrained inverse problems with graph networks. In ICML, 2022.
- [70] David Zwicker. py-pde: A python package for solving partial differential equations. Journal of Open Source Software, 5(48):2158, 2020.